Materials & Design 214 (2022) 110415

Contents lists available at ScienceDirect

Materials & Design

journal homepage: www.elsevier.com/locate/matdes

Experimental and numerical characterization of pure copper heat sinks produced by laser powder bed fusion

Gabriele Sciacca [a,b,*], Mirko Sinico [c,d], Giacomo Cogo [c], Davide Bigolaro [b], Adriano Pepato [c], Juan Esposito [a]

[a] National Institute for Nuclear Physics - Legnaro National Laboratories, 35020 Legnaro, PD, Italy
[b] Department of Industrial Engineering, University of Padova, 35131 Padova, Italy
[c] National Institute for Nuclear Physics - Padova Division, 35131 Padova, Italy
[d] Department of Mechanical Engineering, KU Leuven, 3001 Leuven, Italy

HIGHLIGHTS

- Pure copper complex-shaped heat sinks manufactured via Laser Powder Bed Fusion.
- Liquid cooling characterization by both experimental tests and numerical analyses.
- The heat sink comprising helical channels outperformed lattice structures.
- Rotated lattice structure in respect to freestream direction enhances heat transfer.
- A CFD model was validated by means of cloud-computing.

GRAPHICAL ABSTRACT

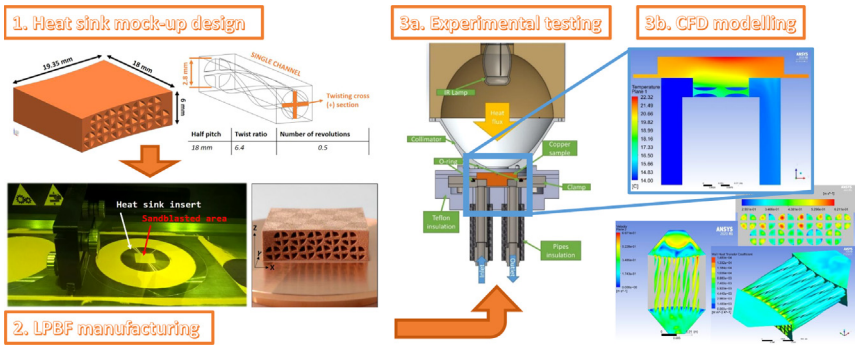

ARTICLE INFO

Article history:
Received 26 August 2021
Revised 10 January 2022
Accepted 18 January 2022
Available online 22 January 2022

Keywords:
Laser powder bed fusion
Pure copper additive manufacturing
Computational fluid dynamics
Heat sink
Nuclear physics
Liquid cooling

ABSTRACT

One of the technological challenges aimed at improving the cyclotron-based radionuclides'(RNs) supply for Nuclear Medicine (NM), is the availability of proper heat sink systems able to remove the large amount of heat deposited during the irradiation stage onto isotope-enriched targets. In this regard, three different non-standard mockup configurations, made of pure copper by means of the Laser Powder Bed Fusion (LBPF) technique, have been tested with an in-house developed experimental apparatus. The experimental characterization has subsequently been compared with numerical results carried out by means of Computational Fluid Dynamics (CFD) simulations. Our numerical model, based on the Re-Normalization Group (RNG) k-epsilon formulation, has shown close agreement (within 1.06 % Mean Absolute Error) with the experimental results, despite the geometrical complexity of the heat sinks prototypes. The combined experimental and numerical approach, together with the flexibility of additive manufacturing production, was proved to be apt for further development of high-efficiency heat exchange applications in this field.
© 2022 The Authors. Published by Elsevier Ltd. This is an open access article under the CC BY license (http://creativecommons.org/licenses/by/4.0/).

1. Introduction

1.1. The LARAMED project

The use of emerging radionuclides' (RNs) (e.g. ^{67}Cu, ^{47}Sc, ^{155}Tb) in Nuclear Medicine (NM), with high potential in cancer treatment,

* Corresponding author at: National Institute for Nuclear Physics - Legnaro National Laboratories, 35020 Legnaro, PD, Italy.
E-mail address: gabriele.sciacca@lnl.infn.it (G. Sciacca).

https://doi.org/10.1016/j.matdes.2022.110415
0264-1275/© 2022 The Authors. Published by Elsevier Ltd.
This is an open access article under the CC BY license (http://creativecommons.org/licenses/by/4.0/).

is strictly dependent to the availability of efficient methods to get cost-effective production routes for these emerging radioisotopes [1,2]. From this point of view, the LARAMED (acronym for LAboratory of RAdionuclides for MEDicine) project, established at the Legnaro National Laboratories of the National Institute for Nuclear Physics (LNL-INFN) in Italy, is setting up a new research facility dedicated to the development of innovative applications of nuclear physics to medicine [3]. It will make use of the BEST 70p high-performance cyclotron, already installed at LNL, for the production of the RNs with the high efficiency typical of the proton-induced nuclear reactions. Since the radioisotope yield is directly proportional to the delivered beam current, one of the key technical aspects of this project is related to the design of a new Target System (TS) able to efficiently drain the full cyclotron beam power impinging on the target. The cyclotron is capable to deliver a beam of accelerated protons with a tunable energy in the range 35–70 MeV and a beam current up to 500 μA [4], resulting in a impinging power up to 35 kW.

1.2. Thermal management of high-current targets

Solid targets usually consist of a layer of an isotopically-enriched material deposited onto a backing plate, where the beam is stopped. With high-current irradiations, the target is encapsulated in a TS to be positioned with a grazing angle in respect to the beam direction, as shown in Fig. 1 [5].

During the bombardment the target itself seals the cooling circuit, while the coolant (typically water) flows along its backside [6]. Such a geometrical configuration has the benefit of spreading the beam power hitting the target surface over a larger spot area, thus reducing the areal power density. However, because of the high cost of the target material, its dimensions are typically limited to few cm. With high-power accelerators, like the BEST 70p, this implies the need to dissipate power densities larger than 1 kW/cm^2.

A heat sink configuration made of a high thermally conductive material can be embedded in the backside of the target, to improve the heat exchange at the wall-fluid interface. From this point of view, copper is generally the material of choice given its excellent thermal properties. Furthermore, it has a higher stopping power with proton beams in comparison to aluminium [7], which allows for the reduction of the backing plate thickness to decrease the related thermal resistance. While many manufacturing routes had been employed to deliver efficient heat sink solutions for target cooling [8–10], Additive Manufacturing (AM) provides more freedom in optimizing the geometry in order to get an additional improvement in heat transfer efficiency. This would be primarily due to the possibility in overcoming the limitations imposed by the traditional manufacturing processes when realizing such a compact-size cooling system. In turn, that would allow for a larger beam current imparted on the target without modification of target dimensions, thus improving the radionuclides' expected yield.

1.3. Additive manufacturing of pure copper

Additive Manufacturing, and more specifically metal AM, has already largely demonstrated how bringing design freedom and near-net shape manufacturing with shorter lead times may turn out to be extremely beneficial to applications involving thermal management and dissipation. Recent reviews, concentrating on products with functional fluid channels [11], heat sinks for applications in electronics cooling [12], or general heat exchanger designs [13], all support the AM positive claims. However, the AM route is not exempted from drawbacks: different metal AM technologies present vastly different process speeds, availability of materials, achievable dimensional accuracy and overall part quality. The

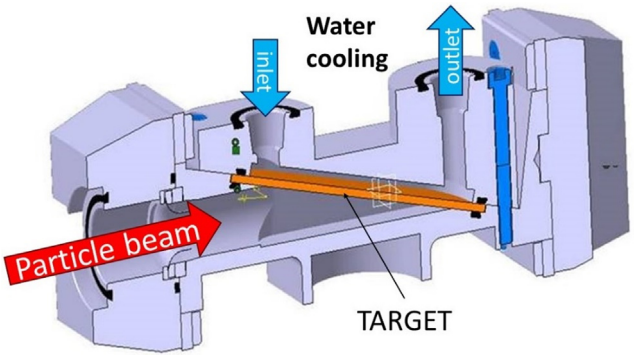

Fig. 1. A typical configuration of a high-current TS (model by IBA-Subatech) [5].

ISO/ASTM 52,900 classifies the single-step metal AM processes in *powder bed fusion*, *direct energy deposition* and *sheet lamination* processing principles [14] Among these three main processes, *powder bed* systems based upon laser melting are identified as the metal AM process resulting with the highest accuracy, materials availability, and in general the larger amount of both academic and industrial research [15–17].

Selective Laser Melting (SLM) or Laser Powder Bed Fusion (LPBF), initially developed in 1995 at the Fraunhofer Institute for Laser Technology (ILT) in Aachen, Germany, has been vastly utilized for heat transfer devices fabrication [18]. However, one major limitation of the technology, in regards to components for heat applications, was the absence of LPBF setups with the capability of processing high copper content alloys. This is due to the inherent high thermal conductivity of the copper material, which hence rapidly conducts heat away from the melt area during LPBF processing, as well as the high reflectivity of copper towards the near-infrared radiation of commonly utilized continuous wave (cw) fiber lasers [19]. The combination of such effects led to sub-optimal LPBF fabrication, with obtained parts presenting lack of fusion defects and, ergo, high porosity contents and weak mechanical properties. The well-known copper dilemma has been recently summarized in different review works [20–23], with also a specific outlook on thermal applications [24]. The important take away of the available literature is that, while the processing of copper alloys is now widely commercially available, only a few industrial realities have successfully marketed LPBF machines ready for the production of nearly-pure or pure copper with low porosity content ($\ll$5 %). This has been reached by either the employment of $\geq$ 400 W power cw fiber laser sources [25,26] or by shorter wavelength (green/blue) lasers [27]. An apt material science approach, where the initial copper powder raw material is purposely modified instead of the LPBF setup, is nowadays also finding its own route towards the additive industry thanks to novel methodologies proposed by e.g. Jadhav et al. [28,29] and Lindström et al. [30] regarding optically absorptive metal-coated copper powders. Finally, Sinico et al. starting from 2017 [31,32] demonstrated how pure copper components with material bulk densities up to 98.1 % are possible to be produced at relative low laser power ($\sim$175 W), by a proper selection of the particle size distribution (PSD) of the raw powder material. A properly engineered PSD skewed towards finer particles was favourable both for an enhanced melting and to unlock the possibility of using small layer thicknesses, down to 20 μm, for LPBF fabrication. While the results were promising and in line with previous researches on different materials [33,34], it was not possible to attain a full density pure copper part and some lack of fusion defects were still detected. However, the proposed method carries the main advantage of being easily scalable to different LPBF systems [35], without any

further machine modifications or chemical treatments of the initial powder. Moreover, the PSD can be easily fine-tuned, either at the source in collaboration with the powder manufacturer, or afterwards by appropriate sieving. At the time of publication of this manuscript, Qu et al. [36] have further corroborated the approach of Sinico et al., achieving 99.6 % dense high-precision LPBF (hp-LPBF) pure copper specimens with a 200 W laser. Their extended design of experiment, performed with a layer thickness down to 10 μm and fine powder, is a confirmation of the feasibility of pure Cu production even with low-end LPBF equipment. Therefore, taking into account the existing LPBF machine constraints for this study, the approach of Sinico et al. was selected as being the most appropriate to successfully produce first mockup prototypes for the work hereby presented.

1.4. Heat sink performance assessment

In order to determine the aptness of this manufacturing process to produce high-efficiency heat sinks for new TS configurations, in this work three compact-size heat exchanging mockups configurations have been tested and compared at the laboratory-scale. For their production a hybrid procedure combining AM and conventional machining has been adopted in order to obtain a robust pure copper metallic structure. Starting from the manufactured samples, a characterization study has been carried out with a test rig specially designed for the purpose. After that, a specific Computational Fluid Dynamics (CFD) simulation model was validated against the experimental results. Such a procedure is quite common when benchmarking the heat transfer efficiency of either heat exchangers [37–40] or heat sinks [41,42] prototypes, for the absence of analytical formulations for newly proposed AM geometries.

2. Materials and methods

2.1. Design of the heat exchanging mockups

Three different mockup prototypes were designed, built and tested, in order to perform an assessment study about their thermal capabilities. The first two were conceived as a metallic lattice structure (referred also as grid), based upon the rhombic dodecahedron thin shape (abbreviated as dode-thin) [43], while the third one as a solid helix channel geometry. The bounding box size of the samples was devised to fit the Heat Sink Prototypes Tester (HSPT) apparatus, which requires every geometry to be integrated with (or built on top of) a special heat sink support plate (Fig. 2), as described in Section 2.3.

Concerning the two lattice samples, the possible applications of LPBF to build lattice, foam-like, structures has been previously explored in literature for both thermal [18,44,45] or mechanical [46–48] purposes; however only scarce research is currently available in LPBF-fabricated pure copper metallic struts [36,49,50]. These structures, if integrated in conformal cooling channels or ducts, can increase the local mixing of the cooling fluid as well as the specific heat-exchange surface, thus markedly improving the heat transfer efficiency [51,52]. In this frame of reference, the advantage of making such structures by means of AM techniques is the capability of manufacturing complex-shaped lattices structures under complete geometrical control. The goal is to further adjust the coolant turbulence level as well as the heat-exchange area in respect to traditionally manufactured copper metal foams.

To that end, the first two mockups were designed having similar geometries, based upon a dode-thin (dodecagonal) 2x2x3 mm cell structure, as shown in Fig. 3. The only difference between the two samples lies in the cell orientation, i.e. the alignment of the cell with the inlet flow: for *lattice type A*, the grid is aligned towards it (*channelling configuration*), while for *lattice type B*, the grid cells are tilted at an angle of 22.5° with respect to the flow direction (*non-channelling configuration*). The second geometrical configuration should guarantee a higher degree of liquid mixing in respect to the former one, since the flow is forced to deviate from its free-stream direction. In any case, the cell structure of the lattice is slightly elongated in the Z direction (height equal to 3 mm) in respect to their width (2 mm), in order to reduce the overhang angle and thus minimizing the amount of dross formation during LPBF manufacturing. Dross and sag [53,54] are indeed common process-related defects, which strongly depend on the AM overhang angle, i.e. the angle between the LPBF build plane and the down facing surfaces of the built geometry, and these defects can be commonly avoided or limited for angles $\geq 45°$. If dross formation is not controlled, it would result in large dimensional deviations and high surface roughness, which is normally undesirable and can progressively decrease the performance of LPBF components [55]. The designed lattice cell presents down facing surfaces with an overhang angle $\geq 47°$.

Alongside these, the third investigated mockup configuration was designed with the purpose of exploring the influence of geometry on constrained fluid flow inside circular channels. The prototype takes inspiration from the twisted tape inserts used in industrial applications, like e.g. heat exchangers, air conditioners, chemical reactors and refrigeration systems [56–58]. These curl flow devices, which are used to generate swirl or secondary flows, are common methods used to achieve an improvement in the heat exchange coefficient, though (as in the metallic foam case) with the drawback of a pressure drop increase. The typical twisted tape inserts are usually made of a different material than the device main body and are inserted (without a welded contact) in the conventionally manufactured tubes or pipes after their fabrication. The sample representing this design, named *helix* mockup, aims at demonstrating how LPBF technique is able to manufacture integrated swirl flow generation structures inside channels in a single production step and as a single-body. The advantages of taking inspiration from a common solution, like the twisted tape, but exploited in such a new AM perspective [59,60] are different: (i) the twisted tape can be applied in the design stage also to complex conformal cooling paths, (ii) the twisting parameters can be varied along the channel length, depending upon the specific performance needs of the cooling system, (iii) the twisting tape is seamlessly connected to the channel walls providing extra conduction towards the bulk material and (iv) both channel walls and twisting tape surfaces may be locally structured [49] to further enhance and control the heat transfer and secondary fluid flow conditions.

The *helix* mockup has been designed as a set of 11 channels arranged on two rows, spaced 3.1 mm centre-to-centre and with a diameter of 2.8 mm. Inside each channel, a twisted cross-shaped flow divider is devised to unfold with the parameters summarized in Fig. 4.

In order to get the experimental characterization as easy as possible, each of the three mockups investigated was attached to a disk heat sink support (Fig. 5), from which the heat flux is delivered. These supports have been manufactured with traditional processes, while the test mockups were grown on top of the support surface with the LPBF additive technique, resulting in an integral part. Therefore, the final test geometries, whose CAD models are shown in Fig. 2, are an integration of a machined Oxygen-Free High thermal Conductivity (OFHC) copper part (in orange) and a additively manufactured pure copper part (in blue), fabricated through a dedicated LPBF platform designed for alignment and fastening of the support in the LPBF build chamber.

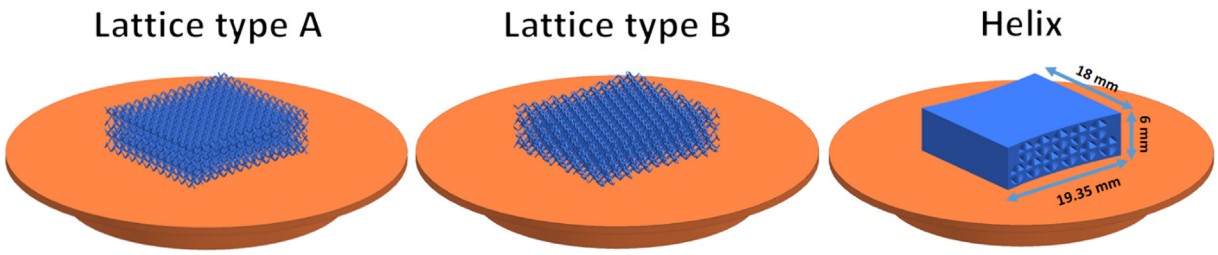

Fig. 2. Trimetric view of the three studied heat exchanging mockups geometries (blue), on top of the supporting heat sink (orange). (For interpretation of the references to colour in this figure legend, the reader is referred to the web version of this article.)

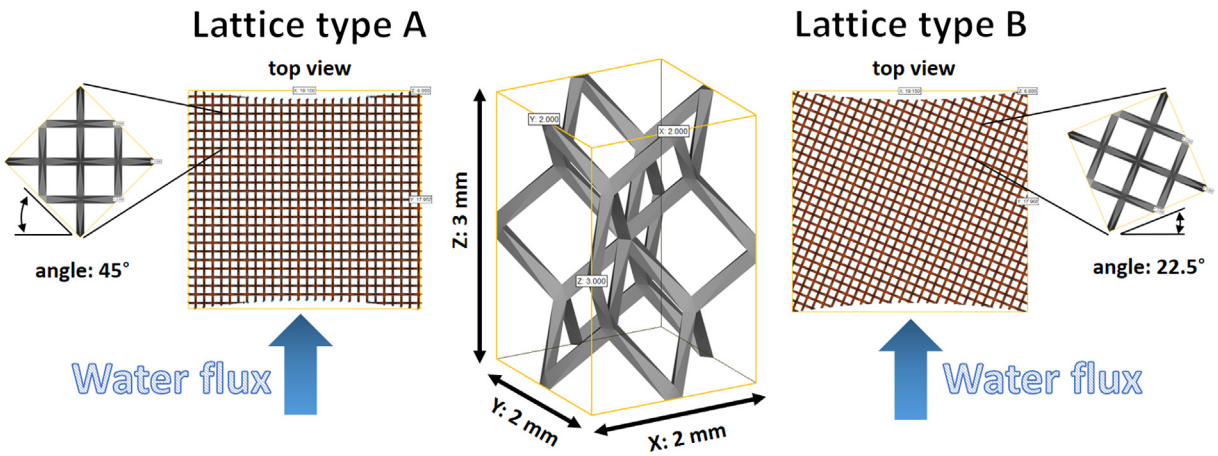

Fig. 3. Top view of the lattice mockups; A type: *channelling* and B type: *non-channelling*, with the dode-thin 2x2x3 mm basic cell unit pictured at the centre.

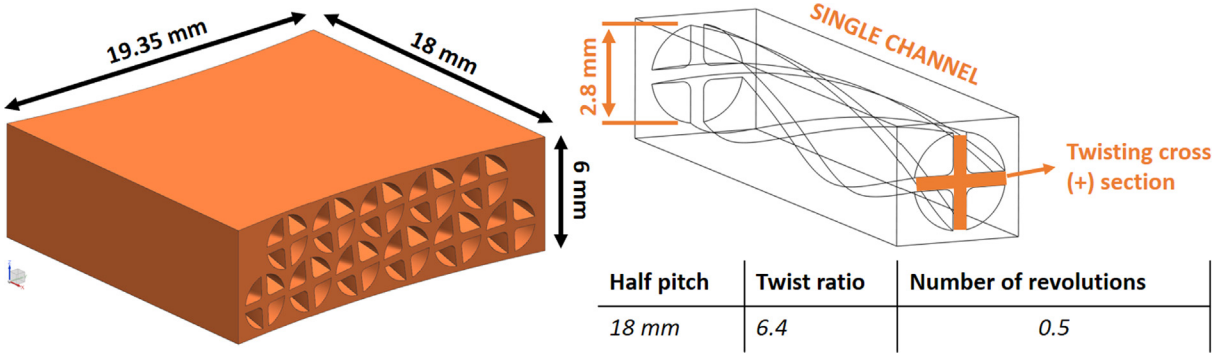

Half pitch	Twist ratio	Number of revolutions
18 mm	*6.4*	*0.5*

Fig. 4. Trimetric view of the *helix* mockup, with shown internal twisted cross parameters.

2.2. Heat sinks LPBF fabrication procedure

The designed test mockups were fabricated with gas atomized 99.8 wt% Cu 10–35 μm powder batch (LPW Technology Ltd) using production parameters (i.e. laser power, laser scanning speed, hatch spacing, scanning strategy and layer thickness) selected after the LPBF optimization described in Section A. The parameters are reported in Table 1. The utilized LPBF system was a SISMA MySint100 PM, working with inert Nitrogen atmosphere.

The process parameter window was chosen taking into consideration a balance between volumetric material fabrication rate and expected copper part density. The combinations listed in Table 1 yield material fabrication rates of 0.30 mm^3/s (helix) and 0.36 mm^3/s (lattices) with an expected copper part relative density as high as ~ 97 % for both types of samples. In addition, both the scanning strategy [61] and the general processing parameters were modulated, depending upon the geometry. For the lattice mockups, the hatch spacing was reduced and the beam compensation offset [62,63] disabled to allow more than one laser scan track inside the infill region of the dode-thin strut section, as shown in Fig. 6. To balance out and keep the volumetric energy density at an optimum level, the laser scanning speed was increased from 375 mm/s to 600 mm/s. This allows both a higher material fabrication rate, and possibly the avoidance of heat accumulation phenomena for thin structures [53,64]. On the other hand, the *helix* mockup was fabricated with a standard parameter combination and scanning pattern, being the geometry not composed of critically thin sections.

Finally, as previously stated in Section 2.1, an ad-hoc LPBF build platform was developed, to be able to grow the mockups directly onto the heat sink conventionally-manufactured backing. This is due to the fact that the sample needs to comply with tight tolerances to be assembled in the experimental HSPT apparatus. Moreover, the heat sink design comprises thin sections, down to 1 mm

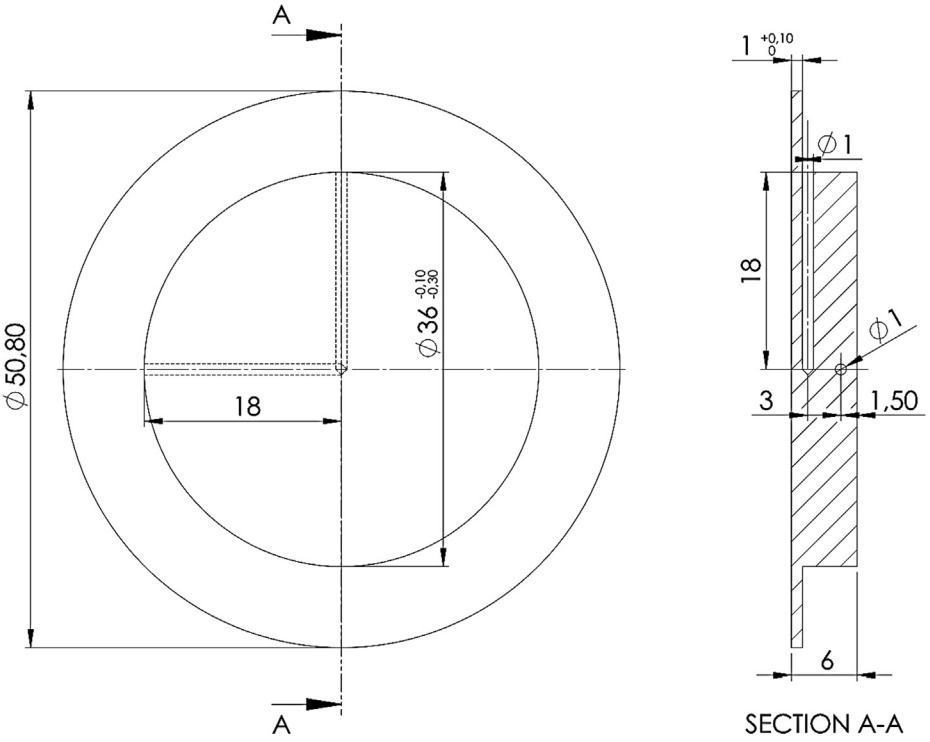

Fig. 5. Technical drawing of the heat sink support. The holes allow for the insertion of thermocouples at different axis depths.

Table 1
LPBF process parameters for the manufacturing of the samples.

Test prototypes	Helix	Lattices
Laser power	175 W	175 W
Laser scanning speed	375 mm/s	600 mm/s
Hatch spacing	40 μm	30 μm
Scanning strategy	Island scanning, 4x4 mm	45° rotate scanning
Contour style	Single scan, external BC*	Single scan, no BC*
Layer thickness	20 μm	20 μm
Volumetric energy density	~ 583 J/mm^3	~ 486 J/mm^3

* BC: beam compensation.

thickness, which have to assure water tightness in operation. The current density reached by pure copper parts produced by LPBF could hinder a perfect sealing for very thin sections, and thus was deemed not suitable for the production of the supporting heat sink. A hybrid fabrication route was used instead, with a build platform designed to host precisely machined (on a parallel lathe) heat sinks, as shown in Fig. 7, right. The build platform and the heat sink backing were conventionally fabricated with the same copper grade, C10100 OFHC. A square region in the centre of the heat sink, Fig. 7 (red area), was sandblasted prior to LPBF processing to reduce as much as possible the risk of back reflection of the incom-

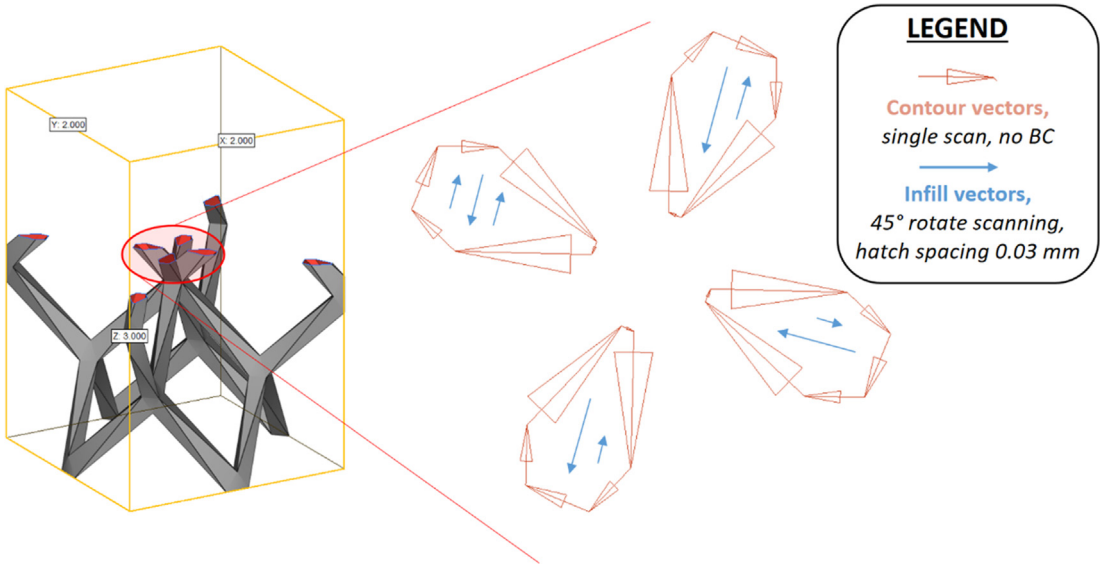

Fig. 6. Example of LPBF laser scanning strategy for the lattice dode-thin structures.

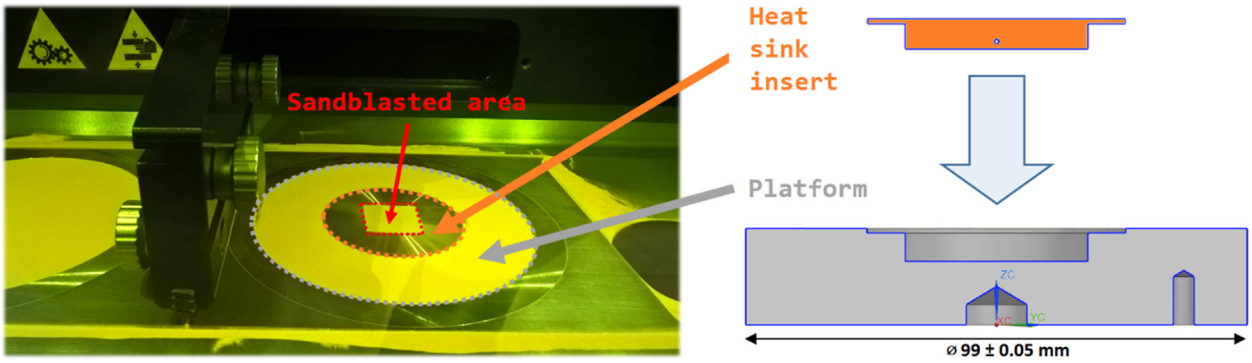

Fig. 7. The SISMA MySint100 PM build chamber before production start; the heat sink, platform and sandblasted area are highlighted. The assembly between the heat sink and the platform is depicted in section on the right-hand side.

ing laser and to enhance the hot bonding quality between the heat sink and the LPBF grown heat exchanging geometries [65].

Total LPBF processing time for the lattice mockups was ∼ 55 min each; total LPBF processing time for the *helix* mockup was ∼ 118 min.

2.3. The heat sink prototypes Tester (HSPT)

The test apparatus was conceived at the INFN-LNL with the purpose to test different heat sinks prototypes produced by metal AM, as described in [66]. A cutaway section of the HSPT setup is shown in Fig. 8, left, with a heat sink mockup mounted inside. A picture of the actual experimental apparatus is also added on Fig. 8, right.

The test section consists of two pipes welded to a steel clamp, which hosts the heat sink body. During the experiments, the heat sink sample dissipates the thermal power applied by an IR Lamp (Inflidge, model HSH-4) only with the chilled water through forced convection. This is due to the PTFE insulation visible in Fig. 8, which also serves as reference for centring the heat sink with the heating source, and the expanded polyurethane sheath covering the circuit's pipes.

The lamp mimics the thermal flux through the actual target's heat sink head during beam irradiation, and its light is focused on the heat sink top surface through an air-cooled parabolic-shaped aluminium collimator, with an internal mirror-like electroplated surface. The water temperature in the loop is regulated with an accuracy of ± 0.1 °C by a Labtech chiller (model H150), which can provide a maximum flow rate of 5 l/min. However, only 1 l/min was dedicated to the experiments, being the rest necessary to cool down the IR lamp. Two PT100 thermo-resistance sensors (RTD) measure the inlet $T_{w,in}$ and outlet $T_{w,out}$ fluid temperatures immediately before and after the test section. The target temperature is instead measured by two K-type thermocouples (first class) inserted into the holes represented in Fig. 5: one, named T_1, in the hole closer to the irradiated surface, while the other one, named T_2, being next to the heat sink printed geometry. Both holes have a depth equal to the radius of the top cylinder, in order to have the thermocouples measuring the temperatures along the sample vertical axis. Regarding the evaluation of the hydraulic conditions in the circuit, the differential pressure among inlet and outlet pipes, as well as the pressure relative to the atmospheric one at the inlet, are measured by two Honeywell pressure transducers, respectively the 24PCFFA6D and the 24PCFFM6G models. The first gauge reads the pressure losses along the length comprehensive of the RTDs, while the second one acquires the upstream pressure before all the sensors. Finally, an ultrasonic flowmeter (Burkert Type, model 8081) is placed after the outlet side of the differential pressure sensor to measure the volumetric flow rate level in the loop.

In all tests carried out, the environmental temperature has always been monitored through a thermocouple positioned nearby the system, while the collimator temperature was checked through another thermocouple in contact with its bottom part. All sensors are connected to an Agilent Data Acquisition Unit (model 34970SDA), controlled by an in-house developed LabVIEW application set up to plot in real-time and store the recorded parameters for off-line analyses.

2.4. Measuring procedure and uncertainty analysis

To test the sensitivity response of the heat sink samples to the provided thermal input, the heating power was applied following a step-increase procedure varying the IR lamp power supply voltage at each step. The last step was constrained by the maximum temperature allowed for the parabolic collimator, which was limited to 200 °C (i.e. about 1/3 of the material melting point) to prevent its thermal damage. At each step all sensors measurements were recorded when the steady-state condition was considered fully achieved, i.e. when thermocouples measurement fluctuations dropped within a range of ± 0.05 °C for at least 5 min. In order to assure repeatability of results under different environmental conditions, a series of tests were performed for each sample. Data analysis was performed after three completed tests were recorded for each specimen.

With such an experimental equipment, a Gaussian light spot profile is thus shone on the top surface of the sample and the heat load diffuse through the sample's volume by thermal conduction; finally, it is removed by the coolant flowing through the heat sink body. Based upon the first principle of thermodynamics, these considerations allow to assume that under steady-state operating conditions the measured dissipated power has to be equal to the heat power entering in the heat sink sample, which hence can be given by Eq. (1) [67]:

$$\dot{Q} = \dot{m} c_{pw} \left(T_{w,out} - T_{w,in} \right) \tag{1}$$

Where $\dot{m}$ is the mass flow rate and c_{pw} the specific heat of the coolant at constant pressure.

Thermal sensors were calibrated in terms of offset against the chilled water temperature, while it was previously assessed that their trend linearly follows the water temperature variations. However, since in Eq. (1) only the temperatures difference appears in the determination of the derived quantity (i.e. the transmitted thermal power), each data point was insensitive to any possible offset error of the absolute temperatures measured by the RTDs. Thus, only the statistical dispersion of measured values was considered as error source, evaluated as ± 0.01 °C. Regarding the thermocouples, an accuracy within ± 0.1 °C has been considered, by

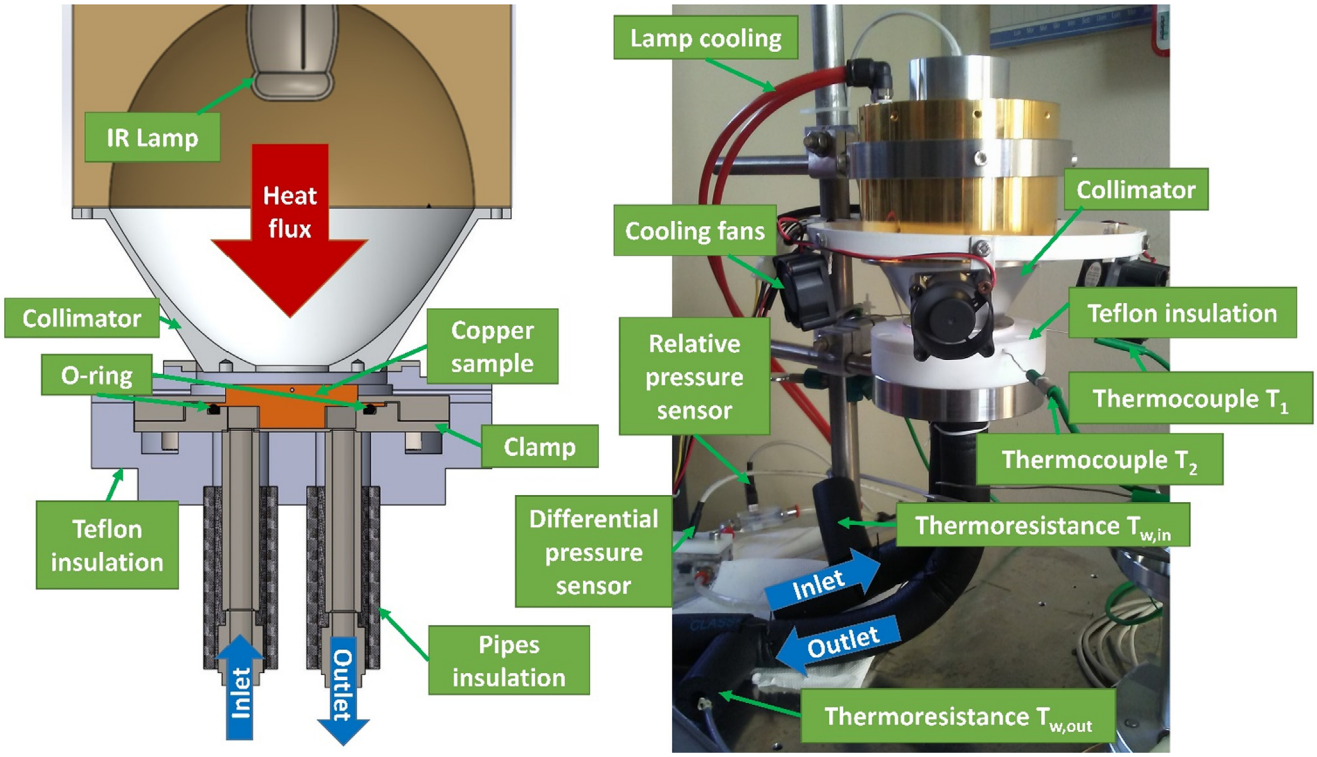

Fig. 8. Left, cross sectional view of the CAD assembly of the HSPT setup; right, a picture of the realized experimental apparatus.

taking as reference the water temperature measured by the chiller. Instead, the uncertainty of pressure and flow rate gauges was assigned from the manufacturers' declared accuracy. Assuming measurement errors were only due to casual effects, the effective value of each parameter was defined as the mean of 50 measurements recorded in sequence during steady-state conditions. Outlier data were discarded from the mean following the Chauvenet's criterion[1] [68]. The final assigned uncertainties are hence grouped in Table 2.

These uncertainties were then used to quantify the error propagation to the transmitted thermal power $\dot{Q}$ with the Kline McClintock formula (2), which in case of unrelated measurements defines the uncertainty of the derived quantity (i.e. $\dot{Q}$) as [69]:

$$i = \sqrt{\sum_{k=1}^{N} \theta_k{}^2 i_k{}^2} \tag{2}$$

with N the number of parameters, appearing in Eq. (1), involved for the determination of the derived quantity, i_k the uncertainty of the k-th parameter, and θ_k the related sensitivity coefficient, given by the first partial derivative of $\dot{Q}$ with respect to the k-th parameter. The uncertainty thus determined was found to be less than 1 % of the measured value for the various performed experiments.

2.5. Numerical model

In order to obtain detailed flow and temperature maps, steady-state numerical simulations were performed employing the ANSYS® Fluent (v.20) tool. For this purpose, the geometrical models of the mockups presented in Fig. 2 were adapted to be apt for the simulations. In particular, the two lattices samples were simplified and shaped following the *cubic isoreticular model* for open cell metal foams [70], by using a cell dimension of L_c = 1.35 mm and pin diameter of 0.25 mm, in order to match the number of pin rows of the manufactured specimens. In the case of the *lattice type B* mockup, the cubic cells were additionally tilted to reproduce as much as possible the original pins' orientation. These adaptations were done to limit the mesh refinement needed to capture the geometrical details of the actual samples, in order to reduce the needs of computational resources. On the other hand, it was chosen to not model the grid as a porous domain to better account for the effect of the individual lattice structures [71,72], which can be relevant when taking into account different cells orientation with respect to the fluid flow. An example of drawn model is reported in Fig. 9, left.

Given the dual thermal and fluid mechanics nature of the problem, the mass, momentum as well as energy conservation laws were considered in the calculations. Turbulence was also modelled, given that the Reynolds number is over the transition value in some regions of the fluid domain. For this purpose, the *Re-Normalization Group* (RNG) variation [73] of standard k-ε was employed, since it offers a better prediction of the streamlines' curvature and convective heat transfer with low Reynolds numbers [74]. The model was used in conjunction with the *scalable wall functions*, in order to avoid the need to adjust the thickness of the first layers of elements at the wall boundaries. Details about the adopted physical model are reported in Section B.2.

Table 2
List of the calculated uncertainties.

Parameter	Uncertainty
T_1 and T_2	± 0.1 °C
$T_{w,in}$ and $T_{w,out}$	± 0.01 °C
$\dot{m}$	± 0.06 l/min
p_{rel} and p_{diff}	± 0.05 bar

[1] This method excludes the measurements which deviation from the average had a probability to be obtained less than 1/2n, with n the number of recorded values

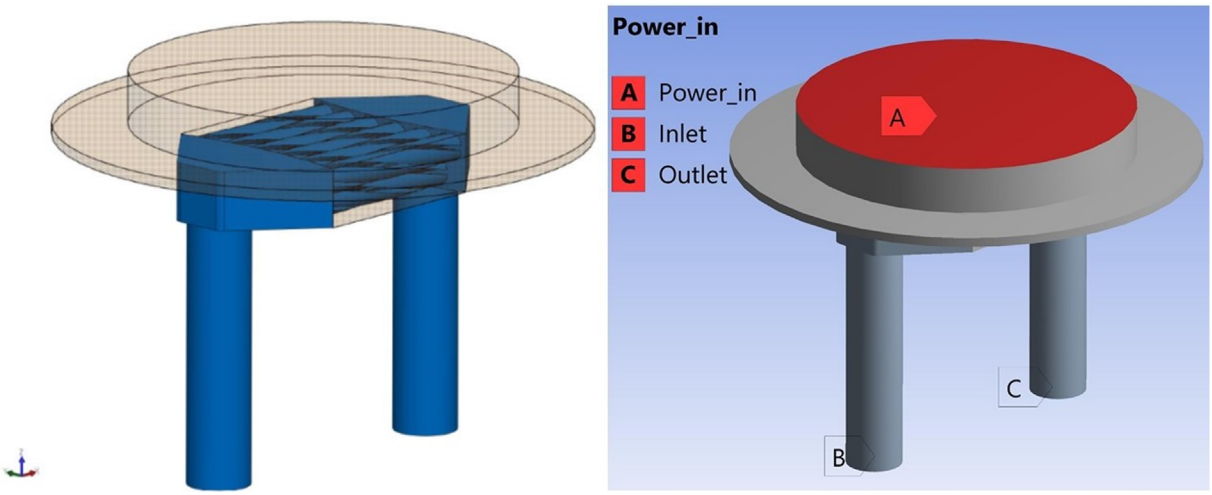

Fig. 9. Left, example of the reconstructed fluid domain inside of the heat sink body (*helix* sample); right, picture highlighting the regions where the boundary conditions were applied for the ANSYS Fluent calculations.

The sample material was set to copper OFHC, that is oxygen-free copper having a high thermal conductivity (i.e. 400 $W \cdot m^{-1} \cdot K^{-1}$). The fluid was instead water, modelled as an incompressible Newtonian fluid. All material properties were kept fixed at their standard ambient values, since temperature and pressure variations in the experiments were negligible. The adopted boundary conditions were as follows:

- Inlet region: the mass flow rate (normal to boundary) $\dot{m}$ along with the inlet water temperature $T_{w,in,}$ were set equal to the measured values reported in Table 3;
- Outlet region: the outflow option, i.e. no condition is applied in terms of pressure or temperature field;
- Power input region: in order to apply the Gaussian heating source provided by the IR lamp, a User Defined Function (UDF) was written to define the input power density as a function of the radial distance r from the central axis:

$$\dot{q}(r) = \frac{\dot{Q}}{2\pi\sigma^2} \exp\left(-\frac{r^2}{2\sigma^2}\right) \quad (3)$$

Where the standard deviation σ was determined by establishing that, in correspondence to the spot radius, the power density is equal to the 25 % of its peak value. This parameter was in turn esteemed from the value reported in the technical specification of Inflidge lamp. Fig. 9, right, shows the corresponding regions of the applied boundary conditions.

The remaining wall boundaries were considered adiabatic. Furthermore, a uniform roughness of 40 μm was assigned to all the sample walls in contact with the liquid. This value, as suggested in [75], was chosen as double of the average of the various walls arithmetic mean roughness $R_{a,i}$, assuming the highest value of R_a reported in [31] as representative of this average.

Domains were discretized through an unstructured mesh composed of first order elements (see Section B.1). All the computations were then performed with the double precision option activated. A pressure-based solver with the coupled algorithm was adopted to improve the numerical stability, while spatial discretization was performed with the second-order upwind scheme to obtain better accuracy. Convergence was reached in less than 300 iterations, fixing for all the computed quantities the maximum residual tolerance to 10^{-3} except for energy, which residual had to be less than 10^{-6} to achieve convergence. Mesh independence was instead evaluated by determining the Grid Convergence Index (GCI) with Eq. (4), which expresses the result variation between different mesh refinements levels [76]:

Table 3
List of the measured quantities used as input data in the ANSYS simulations.

Quantity	Value
$\dot{m}$ [l/min]	1.00 ± 0.06
$T_{w,in}$ [°C]	14.00 ± 0.01
p_{rel} [bar]	1.05 ± 0.05

$$GCI = \frac{f \cdot \varepsilon}{r^p - 1} \quad (4)$$

Here ε denotes the relative error between the results obtained from two different grid spacings (i.e. the mesh size). The parameter r is here the ratio between the fine and coarse mesh sizes, while p being the order of the adopted spatial discretization scheme, and f a safety factor. In this formula p is divided by the number of meaningful dimensions which, in this case, are all the spatial dimensions.

By the fact that additive manufacturing unlocks an almost complete design freedom, the computational effort required to simulate the underlying physics may become a limitation. From this point of view, the numerical characterization can be attained by the use of High Performance Computing (HPC) [77]. Given the complexity of the geometries, in particular, the two *lattice* ones, part of the numerical analyses had to be performed on a platform based on distributed computing. In this study, CloudVeneto [78] was employed as a powerful grid-calculation resource to accurately describe the conjugate heat transfer process. The platform makes available to the user up to 1600 virtual cores of CPUs (Central Processing Units) and 1.6 TB of RAM (Random Access Memory), linked with 1 Gbps network connection. Nevertheless, even resorting to this significant enhancement in resources, the computational power had eventually imposed a restriction in the achievable level of refinement; therefore, a value of 5% for the GCI was chosen as the threshold for mesh convergence. Indeed, the GCI parameter could be used to determine the level of uncertainty in CFD simulations, considering negligible the contribution of either the round-off or the iterative errors [79]. For such a purpose, this value was considered acceptable.

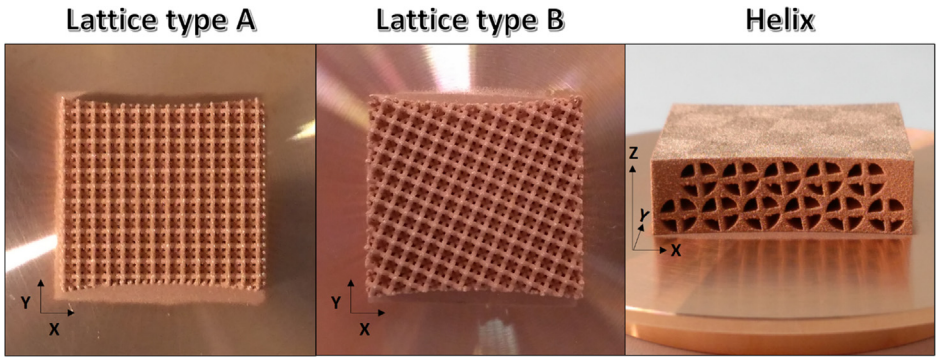

Fig. 10. Pictures of the produced specimens: lattice type A (left, top view), lattice type B (centre, top view), *helix* (right, side view).

3. Results and discussion

3.1. Produced LPBF heat exchanging mockups

The obtained LPBF manufactured specimens, shown in Fig. 10, accurately reproduced the CAD geometries described in Fig. 2. The dimensional accuracies, evaluated through an internal SISMA© benchmark design [32], were respected with a tolerance of ± 40 μm on XY directions (platform plane) and ± 20 μm on Z, the LPBF building direction. Thus, a precise fitting with the experimental apparatus was achieved.

Common and non-critical LPBF geometrical deviations could be noticed after a visual inspection. Since the dimension of the lattices details are nearly in the order of magnitude of the XY tolerance, a slight thickening of the pins which compose these geometries was obtained, due to the partial sintering of small powder particles to their surface. Moreover, minor dross and sag protrusions are present in the *helix* mockup (Fig. 10, right), on the down-facing surfaces of the swirling channels. Both described effects were expected and common for the LPBF AM process [53–55].

The hybrid production method developed for the manufacturing of these specimens enables the reuse of the modified LPBF platform for present and future research on LPBF heat exchanging mockups for the HSPT test rig. This approach comes as a plain example of the current direction of AM, where the additive paradigm is becoming more deeply integrated with the conventional subtractive manufacturing, trying to exploit the advantages of both worlds in the production value chain of complex parts [80–82].

3.2. Experimental measurements and data analysis

A list of the fixed quantities in the experimental tests, used lately as input parameters for the numerical analyses, is reported in Table 3.

The comparison of the three heat sinks prototypes was made at equal entering heat power, in order to find out the best heat sink geometry in terms of heat dissipation performances. The main parameters which can be directly compared in this study are the temperatures T_1 and T_2, in the head position of the heat sink mockups. Hence, the sample which temperatures would be lower at the same heating power level, will be identified as the most performant in terms of heat dissipation capabilities. From the performed tests, which results are summarized in Fig. 11, it was noticed that the heat sink prototype with the *helix* ducts is able to keep its temperature lower than the other prototypes in the investigated conditions. Moreover, the *lattice type B* specimen outperformed *lattice type A*, as it was envisaged from the considerations written in Section 2.1.

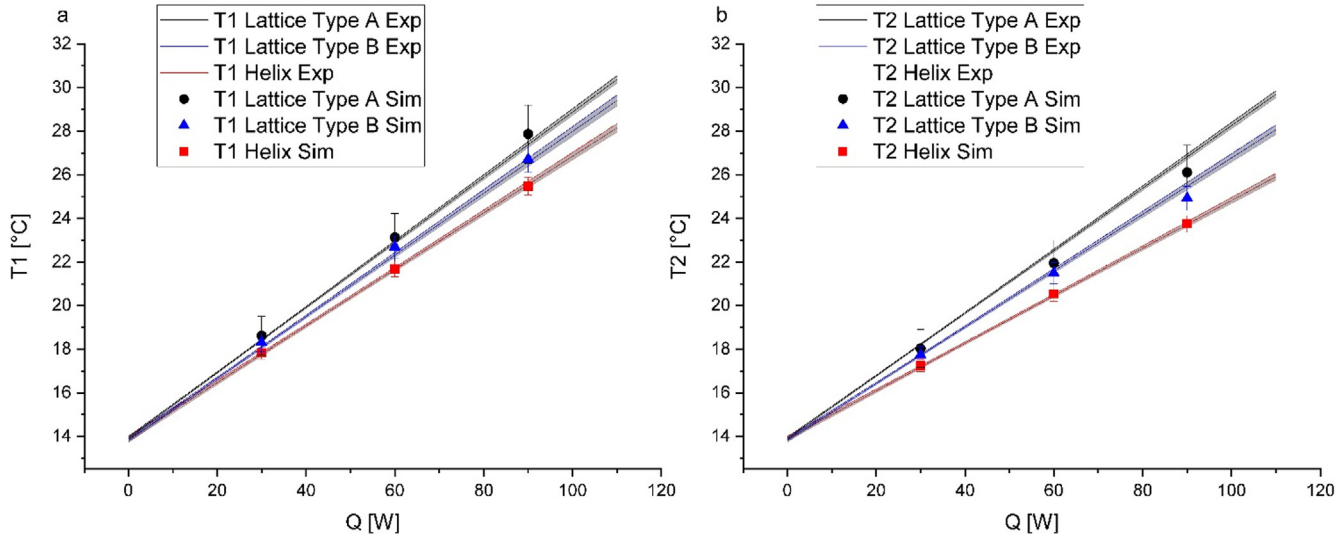

Fig. 11. Plots illustrating the comparison between interpolation of experimental values (Exp) and numerical results (Num) of the temperatures T_1 and T_2.

Regarding pressure drop measurements, a direct comparison of the three samples performances was not possible, since the sensors' accuracy proved to be too low: indeed, the measured value of p_{diff} was always 0.12 ± 0.05 [bar] in either cases, implying that none of the three geometries would cause critical pressure losses (higher than 10 kPa) at the employed flow rate. Furthermore, no influence from the variations of the environmental temperature was noticed in the various tests performed. This in turn means that the measured temperatures of interest were found to be uncorrelated to the environmental one. As a result, the sample temperatures recorded in the tested conditions show direct proportionality to the transferred heating powers, following the predicted response function to the thermal input. Measurements may thus be interpolated with the linear regression fit described by Eq. (5) to extrapolate the sample temperature expected for a given heat power magnitude, which may be used for later comparison with numerical simulations (see Section 3.3).

$$T_i = a_i \dot{Q} + b_i \tag{5}$$

In the above equation, the subscript *i* can be 1 or 2, in reference to the temperatures T_1 and T_2 of the sample. The coefficients a and b of the fit, listed in Table 4, are calculated through the York regression method [83], which accounts for the error on both coordinates. Here b represents the offset of the interpolation line related to the inlet water temperature. Indeed, this quantity fixes the intersection of the fit with the temperature axis, where the heating power $\dot{Q}$ is equal to zero, and hence the sample temperature must be equal to the water one. The resulting interpolation lines for all the tested mockups are drawn in the plots shown in Fig. 11.

From the obtained measurements, an equivalent (or effective) Heat Transfer Coefficient (HTC) parameter can be estimated by considering a fluid–solid heat exchange surface S equal to the joint area between the heat sink geometry and its support (which corresponds to the sandblasted area in Fig. 7, left). In fact, the standard definition of HTC is:

$$HTC = \frac{\dot{Q}}{S(T_{wall} - T_{fluid})} \tag{6}$$

where T_{wall} is the temperature of the solid surface in contact with the fluid, and T_{fluid} the fluid bulk temperature [67]. Approximating T_{fluid} with $T_{w,in}$, and hence with b_2 appearing in Eq. (5), and then T_{wall} with T_2, the equivalent HTC can be determined by the following relation:

$$HTC_{eq} = \frac{\dot{Q}}{S(T_2 - b_2)} \tag{7}$$

Now, given Eq. (5) with i = 2:

$$T_2 - b_2 = a_2 \dot{Q} \tag{8}$$

and substituting it in (7), it yields:

$$HTC_{eq} = \frac{\dot{Q}}{S(a_2 \dot{Q})} = \frac{2.86 \cdot 10^3}{a_2} \tag{9}$$

The HTCs of the various samples thus determined with Eq. (9) are listed in Table 4. They correspond to the heat transfer rate which the coolant must realize to obtain the same fluid–solid temperature gap in absence of the heat sink body. Its accuracy interval is determined with Eq. (2) from the standard error of coefficient a_2, resulted from the fit done with the York regression method.

Given the relatively low flow rate used during the experimental campaign, the values reported witness the high performance of the manufactured heat sinks.

3.3. Model validation

The calculated GCI parameter for each of the three samples at the power input value of 60 W are shown in Table 5. In the same table are listed the characteristics of the meshes used to calculate the GCI with Eq.(4). The computed value of T_1 for the different mesh sizes was taken to determine the relative error ε with Eq.(10):

$$\varepsilon = \frac{T_{1,coarse} - T_{1,fine}}{T_{1,fine}} \tag{10}$$

where the subscripts coarse and fine are referred to the correspondent mesh refinement level. Moreover, a safety factor f = 3 was adopted, as advised when considering only two mesh sizes [84].

As it can be noticed from Table 5, the required number of nodes to achieve convergence for the lattices was one order of magnitude higher than the one needed for the *helix* sample. This is expected and directly related to the presence of many geometrical details in the structure of the two grids.

Since the evaluation of heat transfer efficiency is of primary interest for the application of this study, the validation of the proposed numerical model was done taking the temperature values as reference. Table 6 reports the relative errors e_r between the interpolated experimental values T_{exp} and the numerical results T_{sim} for different entering power magnitudes, determined as follows:

$$e_r = 100 * \frac{T_{sim} - T_{exp}}{T_{exp}} \tag{11}$$

Table 4
Calculated linear regression coefficients with corresponding standard error estimates, and estimated equivalent HTCs with their accuracy interval.

Specimen	$a_1 \pm e_{a1}$ [°C W^{-1}]	$b_1 \pm e_{b1}$ [°C]	$a_2 \pm e_{a2}$ [°C W^{-1}]	$b_2 \pm e_{b2}$ [°C]	HTC_{eq} [W m^{-2} K^{-1}]
lattice A	0.149 ± 0.001	13.936 ± 0.032	0.144 ± 0.001	13.909 ± 0.030	(1.98 ± 0.01) ·10^4
lattice B	0.142 ± 0.001	13.823 ± 0.051	0.129 ± 0.001	13.834 ± 0.045	(2.21 ± 0.02) ·10^4
helix	0.130 ± 0.001	13.878 ± 0.071	0.109 ± 0.001	13.904 ± 0.058	(2.62 ± 0.02) ·10^4

Table 5
Mesh parameters and determined Grid Convergence Indexes with $\dot{Q}$ = 60 W.

Specimen	Mesh size [10^6 nodes]		Minimum orthogonal quality		GCI [%]
	Coarse	*Fine*	*Coarse*	*Fine*	
lattice type A	28.3	48.1	0.18	0.17	4.87
lattice type B	19.0	27.1	0.12	0.13	2.23
helix	2.7	4.6	0.28	0.23	1.62

Table 6
Numerical and experimental results comparison, with related uncertainties.

Sample	$\dot{Q}$ [W]	T_1 [°C]		T_2 [°C]		e_r [%]	
		Num	*Exp*	*Num*	*Exp*	T_1	T_2
lattice type A	30	18.72 ± 0.91	18.37 ± 0.03	18.11 ± 0.88	18.17 ± 0.03	1.03	−1.10
	60	23.44 ± 1.13	22.74 ± 0.06	22.22 ± 1.07	22.34 ± 0.05	0.87	−2.66
	90	28.16 ± 1.37	27.11 ± 0.09	26.33 ± 1.27	26.51 ± 0.08	1.60	−2.83
lattice type B	30	18.31 ± 0.41	18.01 ± 0.05	17.74 ± 0.40	17.66 ± 0.04	1.61	0.23
	60	22.69 ± 0.51	22.02 ± 0.09	21.49 ± 0.48	21.32 ± 0.08	2.12	−0.37
	90	27.04 ± 0.60	26.03 ± 0.14	25.24 ± 0.56	24.99 ± 0.12	1.10	−2.00
helix	30	17.83 ± 0.29	17.78 ± 0.04	17.25 ± 0.28	17.18 ± 0.03	0.22	0.41
	60	21.68 ± 0.35	21.56 ± 0.08	20.53 ± 0.33	20.37 ± 0.07	−0.05	0.39
	90	25.48 ± 0.41	25.33 ± 0.12	23.75 ± 0.39	23.55 ± 0.10	−0.43	0.13

In Eq.(11) the values T_{exp} were determined with Eq. (5) using the coefficients listed in Table 4, while T_{sim} are the computed numerical values $T_{1,fine}$ and $T_{2,fine}$ with the refined meshes.

An accuracy interval is then assigned to both the numerical and experimental values reported in Table 6. For the former the uncertainty is given by the GCI of Table 5, as previously stated in Section 2.5. Instead, the latter corresponds to the interval covered by the confidence band after the York regression of the experimental data (see Section 3.2), for the heating power magnitude to which e_r is referred. Furthermore, the Mean Absolute Error (MAE) can be then determined from the average of the absolute values of reported e_r. This yields a MAE of 1.00 % for T_1 and of 1.12 % for T_2, and a global MAE of 1.06 %. The latter is simply given by the average of the two MAEs, and is a commonly used estimator for the accuracy of the numerical model. The residual deviance between experimental and numerical results could be ascribed either to the uncertainties introduced in the experimental procedure and in the computational model, which are both accounted by the respective error band. Hence, this has been considered sufficient to validate our numerical simulations in the investigated conditions, also considering the model simplification introduced to simulate the two lattices and the assumption of a uniform roughness over the heat sinks' walls. Fig. 11 gives a graphical representation of the comparison between measurement interpolations and numerically calculated values, from which is possible to notice the superposition of their error bands.

This supports the use of such CFD tools, in particular the Fluent package, in the development of new concepts of heat sinks, leaving the possibility to perform an optimization with the exploitation of HPC resources like the one used in this work. In this way, it will be possible to explore the influence of geometrical parameters not investigable in other ways, like the pins' orientation of the lattices' structure in respect to flow direction. After the determination of an optimal configuration, a prototype could be manufactured to be tested with the presented HSPT rig, leading to a further reduction of the required experimental proofs. Once validated, such a modern approach of heat sink design based on cloud computing could be a promising procedure to successfully obtain a deep understanding of the geometry influence in the heat transfer process. That would provide new ways towards further optimization of heat exchanger geometries like the ones here considered, in order to find out the best configuration for the TS before the upscaling process at full cyclotron beam power.

The validation of the numerical results also confirms the reliability of the manufacturing process, given the approximation of considering the whole sample made of copper OFHC with isotropic thermal conductivity, besides neglecting a possible thermal conduction resistance between support and heat sink. In future, further studies will be carried out to extend the validation to different flow regimes characterised by higher Reynolds numbers.

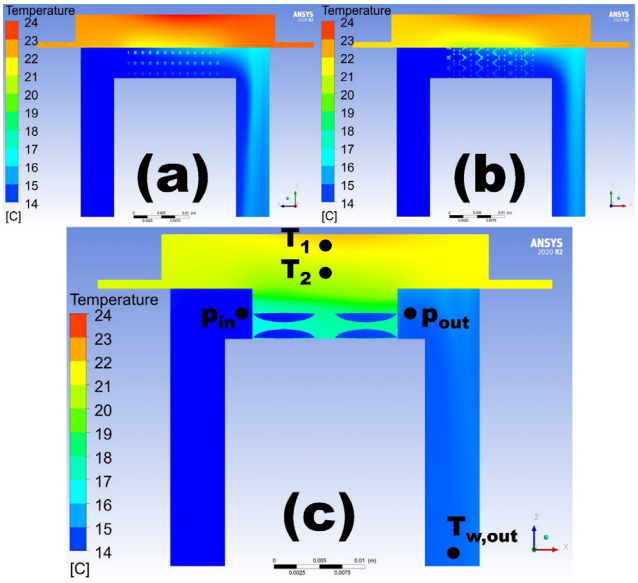

Fig. 12. Colour maps of temperatures distribution (cutaway views along beam pipes axis) for the grid *lattice type A* (a), tilted grid *lattice type B* (b) and *helix* (c) samples, for $\dot{Q}$ = 60 W. Water enters from the left hand side.

3.4. Numerical results

The map distribution of the most important parameters, i.e. temperature and velocity fields, along with the computed HTC, are plotted in Figs. 12–15. These results are obtained with the fine mesh sizes (reported in Table 5) for the case of an applied heating power of 60 W. The nodal HTC values were assigned by Fluent for each fluid cell's face in contact with the solid domain following Eq. (6): in this case S refers to the area of the face, $\dot{Q}$ to the heat flux passing through it, and T_{wall} and T_{fluid} to the temperatures of the respective solid and fluid cells connected through that face [74]. Fig. 12c shows the points where the values of T_1 and T_2 are picked up to be compared with the experimental results. Along with these temperatures, the water temperature $T_{w,out}$ was checked to assess that the thermal balance between applied and dissipated power was always fulfilled throughout all performed computations. The same figure also underlines a clear asymmetry of the temperature distribution inside the heat sinks head. This is in agreement with what is expected by the applied boundary conditions, since water is heated while flowing through the heat sink up to a temperature quantifiable with Eq.(1), while the local HTC, extrapolable from the plot in Fig. 13, is lower at the outlet. The combination of these two factors cause that the tested geometries acquire an increase in

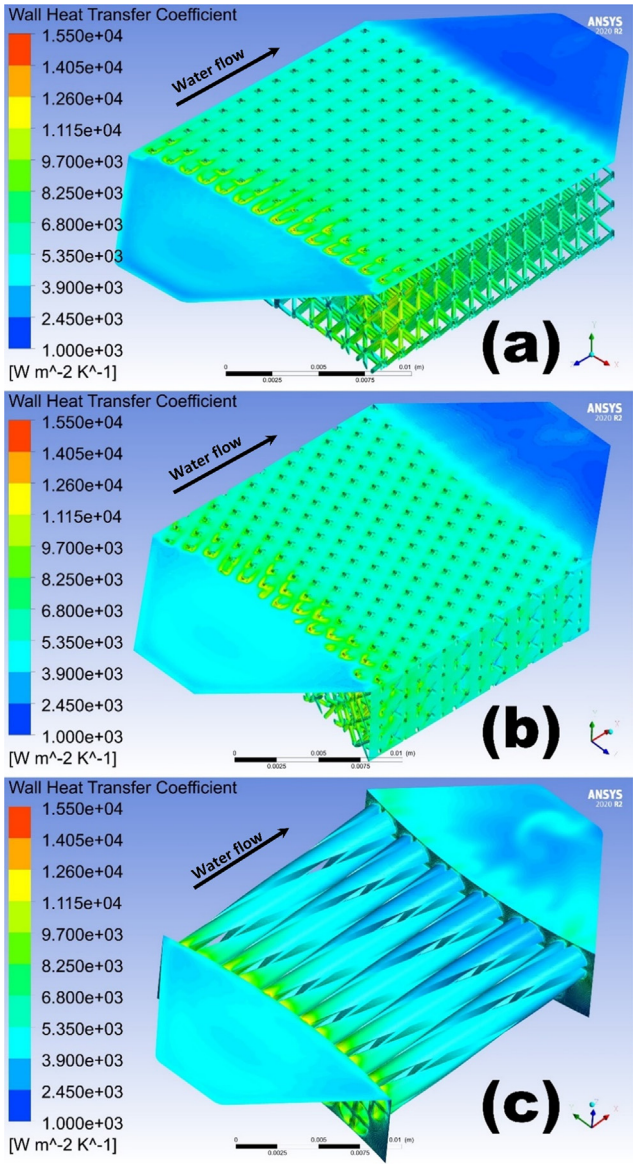

Fig. 13. Colour maps of wall HTC for the grid *lattice type A* (a), tilted grid *lattice type B* (b) and the *helix* (c) samples, for a hitting power level $\dot{Q}$ = 60 W.

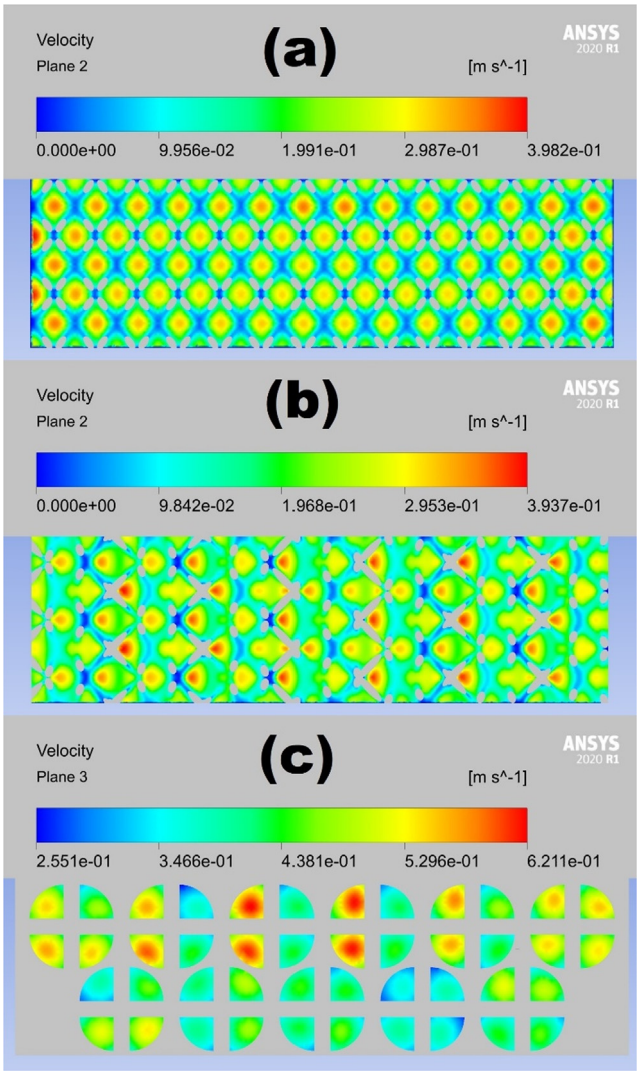

Fig. 14. Transversal cutaway views of velocity field at the mid plane for the *lattice type A* (a), *lattice type B* (b) and *helix* (c) samples. All the legend ranges are referred to local values (i.e. on the plotted plane).

temperature in the part near the outlet arm, thus generating an asymmetry in the radial temperature gradient. For example, considering *lattice type A* and $\dot{Q}$ = 60 W, the average wall temperature would be ≈ 22.2 °C at the inlet side, and ≈ 22.9 °C at the outlet.

Fig. 14 offers a direct comparison of the flow behaviour for the analysed specimens. While in Fig. 14a the flow velocity is higher in the centre of the grid gaps, this is not the case for *lattice type B* (Fig. 14b), where water is forced to follow a wavy pattern to cross the pins. As a result, in this situation the stream is concentrated in the zones where the path between inlet and outlet of the heat sink is shorter. Similarly, from Fig. 14c it may be noticed that the points of higher water speed are deviated from the channel core thanks to the swirl flow induced by the helical curvature. In the same figure it is also possible to see that the *helix* sample is characterized by a spread in flow velocity distribution across the various ducts. In fact, the fluid speed ranges from 0.3 m s^{-1} up to 0.6 m s^{-1} along this section. This effect can be also related to the low flow rate involved in the study, and it is expected to be mitigated at larger Reynolds numbers.

Table 7 summarizes the numerical results obtained for the three heat sink geometries. The value of the pressure drop Δp was determined from the values of p_{in} and p_{out} collected at the points illustrated in Fig. 12c. As it can be noticed, the computed value of Δp were lower than the pressure sensors' accuracy. This is coherent with the experimental results, where no appreciable variation in its measurement was found among the tested prototypes. The average Reynolds numbers Re were instead determined with the known Eq. (12) [85]:

$$\mathrm{Re} = \frac{\rho v D}{\mu} \tag{12}$$

Where:

- ρ is the coolant density (approximated to 1000 kg m^{-3});
- D is the characteristic length;
- v is the mean bulk flow speed inside the heat sink;
- μ is the dynamic viscosity of the fluid (approximated to 10^{-3} Pa s).

For the *helix* prototype, D is equal to the channel hydraulic diameter (≈ 0.9 mm). Meanwhile, in the case of lattice mockups,

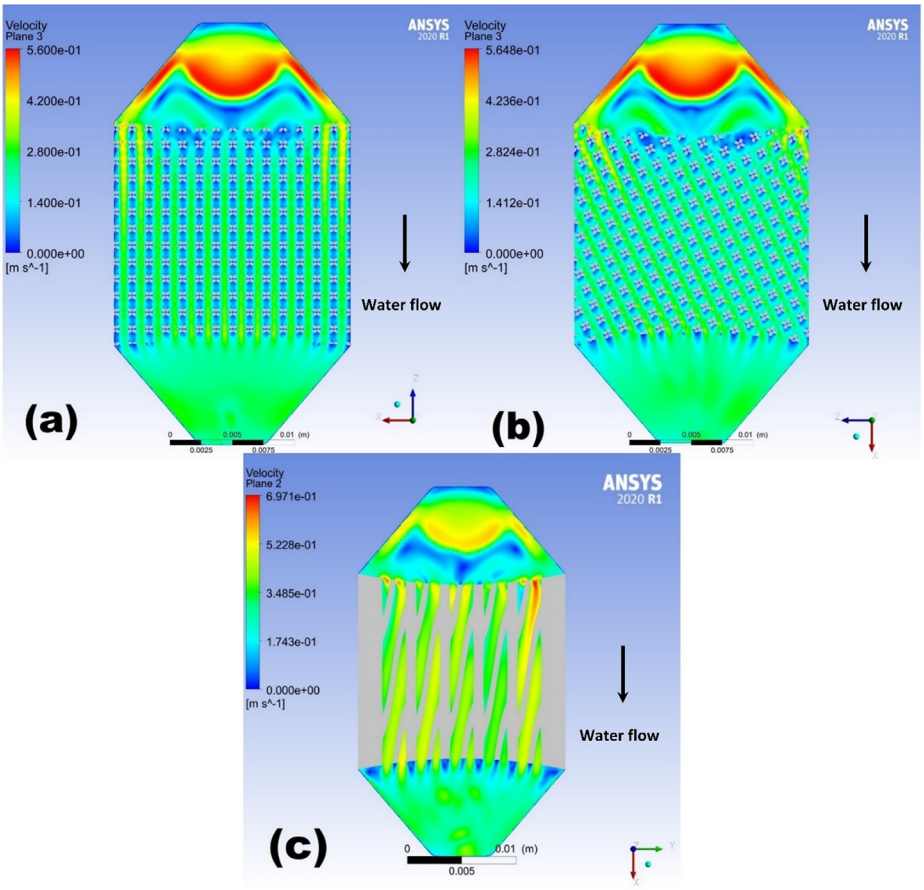

Fig. 15. Longitudinal cross-section of velocity-field maps at a distance of 2 mm from the base of the heat sink support, for the *lattice type A* (a), *lattice type B* (b) and *helix* (c) samples. All the legend ranges are referred to local values (i.e. on the plotted plane).

Table 7
Computed numerical values for $\dot{Q}$ = 60 W.

	Lattice type A	*Lattice type B*	*Helix*
T_1 [°C]	23.44	22.69	21.68
T_2 [°C]	22.22	21.49	20.53
Δp [Pa]	470	576	234
v [m s^{-1}]	0. 28	0.29	0.50
Re	590	611	397
A_s [mm^2]	3755	3766	2880
HTC [W K^{-1} m^{-2}]	6831	7322	4701

D may be obtained from the porosity ε (≈ 0.87) of the samples and the cell dimensions by Eq. (13) presented in [70]:

$$D = L_c \frac{2\varepsilon}{\sqrt{3\pi(1-\varepsilon)}} \tag{13}$$

In Table 7, HTC denotes the average value determined from the numerical nodal ones along the heat sinks' surfaces. It's worth noticing that, even if the two lattices have a wider heat exchange area A_s and achieve a higher average HTC (as visible in Fig. 13), the copper temperatures resulted to be higher. This can be related to the limitation in the heat transferred to the heat sink body for the restriction induced by the pin cross-section, as it can be noticed also from the higher thermal gradient along the grids' struts in the plots of Fig. 12.

Indeed, effective thermal conductivity of a porous domain is related to its lattice structure [44], and higher porosities cause a smaller cross-section available for the heat passage. Consequently, it is possible to state that the increase in heat exchange area offered by the grid geometry, in respect to the *helix* sample, does not mean a corresponding improvement in the heat dissipation. On the contrary, this could adversely affect the heat sink performance by restraining the heat transfer through the heat sink body, if the grid is not properly designed. This, despite the increased heat exchange between the coolant and the heat sink body due also to liquid mixing inside the grids' channels. Moreover, a pressure drop increase may be obtained even if the fluid velocity is lower, since the liquid flow is constantly perturbed by the continuous cross-section variation generated by the grid structures. Finally, one can observe that *lattice type B* achieved a higher HTC in respect to *lattice type A*, which accounts for the better performance of the former, confirming the predictions. This is due to the higher flow path perturbations induced by the lattice's pins to the free-stream flow direction (*non-channelling*), as illustrated in Fig. 15b. Hence, a tilt of the grid in respect to the fluid flow has confirmed to be advantageous for the heat transfer efficiency, at the expense of the impedance, leading to a slight increase in pressure drop.

These findings will thus be the reference for future investigations on the identification of the best design choice, both regarding the geometry and the parameters that defines it. This includes, for example, the performance dependence to the pins' diameter and orientation in the case of the grid geometry, or the twisting ratio and channels number for the helical ducts. From this point of view, given the positive validation reported in Section 3.3, the results of this work open the possibility for the development of an advanced optimization procedure for complex-shaped and high-performing heat sinks for target cooling solutions. Indeed, a first selection of suitable shapes can be initially screened via simulation runs on high performance computing platforms by just exploring the influ-

ence of the various involved geometrical parameters; promising designs identified in this way can be subsequently fabricated and tested, first, in laboratory test-benches, like the hereby described HSPT apparatus and, subsequently, upscaled to full power validation. The short lead-time and geometrical freedom are necessary qualities for the fabrication steps of both future heat sink mockups and upscaled target cooling solutions. Therefore, it can be envisioned that AM processes, and in particular the LPBF technique, could possibly play a major role in the upcoming years to achieve the goal of a compact and high performing TS, for the final mission of advancing nuclear medicine and cancer treatments with a high throughput of novel RNs.

4. Conclusions

The lack of novel radionuclides readily available is refraining the development of new and more efficient radiolabelled molecules for the diagnosis and treatment of cancer. One of the major impediments in their spreading resides in the problem of thermal management for solid Target Systems (TS). With this work, the LARAMED project aims to fill this gap, by exploiting the potential of metal AM technology in overcoming the technical constraints of traditional manufacturing in complex heat exchanger production. Considering the published developments for AM copper fabrication, three prototypes of heat sinks made in pure copper were manufactured with the LPBF technique. The proposed production approach takes advantage of an engineered distribution of copper powder, combined with a suitable selection of LPBF parameters and a hybrid production process, resulting in integrated, complex-shaped heat sink solutions.

One *helix* type heat sink mockup, characterized by helical twisting channels, and two *lattice* ones, consisting of a rhombic dodecahedron thin structure, were manufactured. In particular, the two grid configurations differ from each other for the cells alignment with respect to the freestream fluid direction. The mockups have been modelled and characterized in detail by means of numerical simulations and experimentally evaluated with an in-house built test rig devised for the purpose. All samples resulted to be performant heat sinks, achieving an effective HTC, i.e. the inverse of the heat sink thermal resistance with the coolant, higher than 19 $kW{\cdot}m^{-2}{\cdot}K^{-1}$ (up to 26.2 $kW{\cdot}m^{-2}{\cdot}K^{-1}$ for the *helix* sample). An additional goal of the assessment was a direct comparison of the prototypes' thermal performances. For the considered fluid dynamic regime, the *helix* mockup exhibited the highest heat dissipation capability, providing the overall lower sample temperature distributions at equal heating power and coolant flow rate. This was related to the higher heat transfer efficiency of its geometry in comparison to the two grids (HTC_{eq} = 19.8 $kW{\cdot}m^{-2}{\cdot}K^{-1}$ for *lattice type A* vs. HTC_{eq} = 22.1 $kW{\cdot}m^{-2}{\cdot}K^{-1}$ for *type B*). As expected, the non-channelling configuration of the grid (i.e. with lattice axis tilted with respect to the flow direction) exhibited an improved heat transfer efficiency, due to the more intense perturbations induced to the flow path, promoting fluid mixing.

Finally, a CFD model based on the k-ε RNG formulation was validated, with the use of cloud computing, to bring an accurate characterization of the flow regime and heat transfer process. In the proven conditions, it has shown to provide high-fidelity results for complex geometries as the ones here studied, even in combination with the *cubic isoreticular model* for lattices definition. Indeed, thanks to its ability in forecasting the heat transfer rate with varying Reynolds numbers in rapidly-strained flows, our CFD model has yielded numerical results having less than 3 % of relative deviation with the experimental results, with a Mean Average Error of 1.06 %.

Overall, this study has demonstrated the suitability of the LPBF technique to manufacture complex-shaped pure copper geometries for liquid cooling of TS, and the possibility of predicting their performance with detailed CFD analyses. Considering this last point, in this study numerical simulations have proven to be an essential instrument in the identification of the root causes for dissimilar performances in distinct heat sinks geometries, like the ones investigated. Therefore, this production-validation chain could be applied to the future development of an efficient TS for the LARAMED project, opening the opportunity to further optimize the production yield of the radioisotopes.

Data availability

The raw/processed data required to reproduce these findings cannot be shared at this time as the data also forms part of an ongoing study.

Declaration of Competing Interest

The authors declare that they have no known competing financial interests or personal relationships that could have appeared to influence the work reported in this paper.

Acknowledgements

This research was funded by MIUR in the framework of the TERABIO project. We would like to thank Dr. Hanna Skliarova and Dr. Sara Cisternino for the idea of the HSPT assembly, and the LNL mechanical workshop for the manufacturing of the whole test rig. We are also grateful to Alessandro Zanon for the installation and maintenance of the electronic part, and to Dr. Carlos Rossi Alvarez for the continuous support and precious hints. Additionally, this research was partially funded by the project 5687-1-2121-2015 POR FSE 2014-2020 Veneto "Implementation and characterization of advanced additive manufacturing techniques, applied to the production cycle of the mechanical industry in the Veneto Region". The industrial partners SISMA SpA. and Officina Dei Materiali SaS are kindly acknowledged for their support in the production of the LPBF fabricated copper specimens. We would also like to express our gratitude to Marco Romanato and all the mechanical design and manufacturing team at the National Institute for Nuclear Physics - Padova Division. Finally, CloudVeneto (www.cloudveneto.it) is acknowledged as well, for the use of computing and storage facilities, and for the provided assistance in their configuration.

Appendix 1. Optimization of LPBF pure copper fabrication

The fabrication of pure copper was investigated on a SISMA MySint100 PM LPBF machine. The selected system includes a 200 W fibre laser with a spot size on the focal plane of 30 μm. Inert atmosphere during processing was Nitrogen with a maximum O_2 content less than 100 ppm. Gas atomized 99.8 wt% copper powder (with 0.07 wt% residual O_2) was purchased from LPW Technology Ltd, with a distribution range of around 10–35 μm. The powder size distribution had been engineered to overcome the difficulties encountered in the AM laser production of pure copper [31]. The performance of the powder, in regards to LPBF fabrication, was compared to a standard 15–45 μm particle size distribution. Laser diffraction and scanning electron microscopy (SEM) analyses were initially performed on the powder batches, to confirm their distribution range and qualitatively show their high sphericity (Fig. 16).

The powder optical reflectance was also assessed, through a Jasco V-570 spectrophotometer with integrating sphere ISN-470, and amounts to a reflectance of ~ 70 % towards the 1070 nm radiation, which is the near-infrared wavelength of the fibre laser

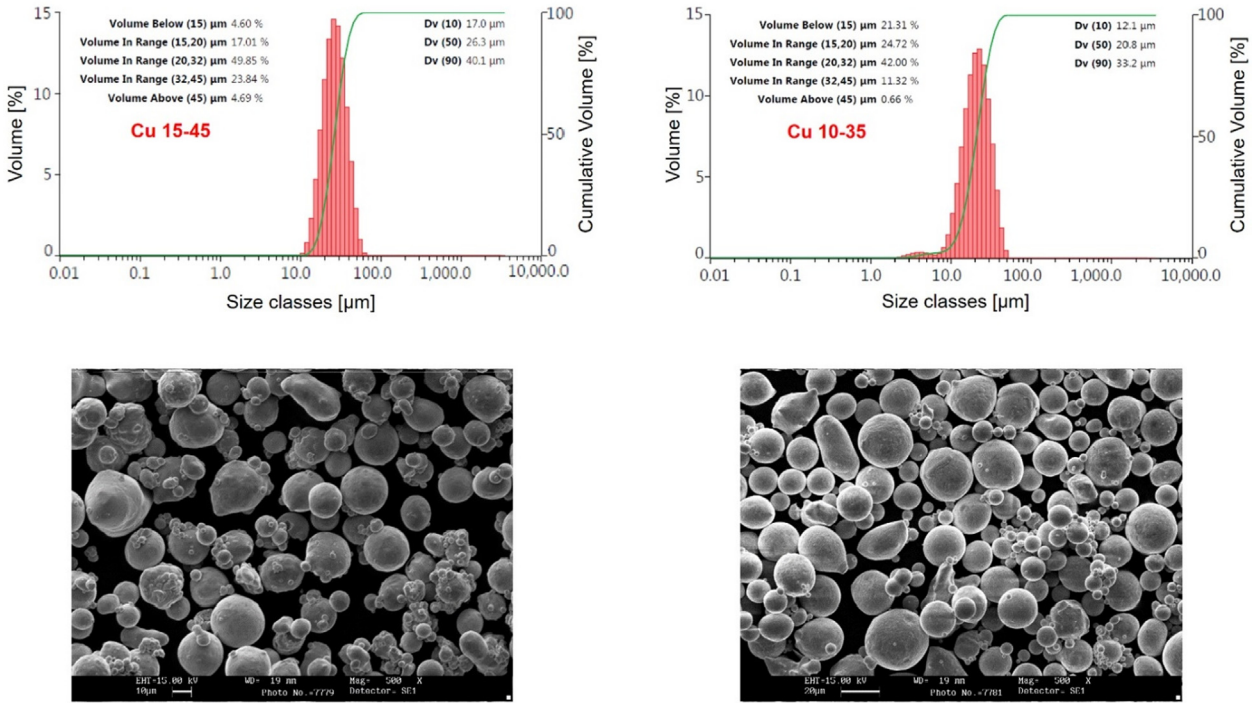

Fig. 16. Particle size distribution (PSD) of the selected pure copper powders, from laser diffraction analyses (provided by LPW Technology Ltd); corresponding SEM image below each PSD (500x magnification); from [31].

installed in the SISMA LPBF machine. The well-known low absorptivity of the laser input energy is directly connected to the difficulties in the LPBF processing of copper, and, as reported in [86,87], the total reflectance becomes even higher when the material goes from a powder state to a liquid melt, reaching coefficients as high as 97 % and staying at an average value of 90.1 % (since this property is function of the irradiated surface temperature).

The performance of the two copper powders was evaluated with the LPBF production of cubic specimens 10x10x10 mm, with both standard Cu 15–45 μm and Cu 10–35 μm powders, at a fixed laser power of 175 W. In order to avoid the formation of lack of fusion defects, layer thickness was also kept fixed at the minimum setting available on the SISMA machine, i.e. 20 μm. Hatch spacing and scanning strategy were varied during first internal assessments performed at the company SISMA SpA, with tested hatch distances of 30, 40 and 50 μm. For the following presented results, hatch spacing was selected as a fixed 40 μm distance, and scanning strategy was zigzag (bi-directional) within each layer, with a 90° scan rotation angle between the successive layers. An initial assessment of the stability of the melt pools at a scan speed of 500 mm/s can be appreciated on the following SEM image of the top surface of a 10x10x10 mm sample fabricated with the 10–35 μm powder batch, Fig. 17. The hatch spacing was set at 110 μm to appreciate the single scan tracks.

Considering a desired overlap of 30 % between adjacent tracks and the measured scan track width (~60.5 μm), the selected hatch spacing matches the sought outcome. However, while stable fusion is reached with continuous tracks, it is already perceivable how some balling, recesses and weld instability remain.

LPBF feasibility was therefore investigated at different laser volumetric energy density conditions ($E_v = P/(v \times h \times t)$, with P laser power, v laser scan speed, h hatch spacing and t layer thickness). Considering the fixed parameters described above, only laser scan speed was tuned in this design of experiment (DoE). The performance of the optimized Cu 10–35 μm powder batch was compared to a smaller DoE performed with the Cu 15–45 μm powder batch. 10x10x10 mm cubic samples were produced with the different parameter sets. Relative density measurements were performed, after careful cutting and polishing of the cubes [88], with optical microscopy. The studied optimization is summarized in the following graph, Fig. 18, where the obtained relative density is plotted against the employed laser energy density E_v.

A maximum of 88.4 % relative density is attained with the Cu 15–45 μm powder, a result consistent with the previous published literature on LPBF of pure copper at low laser power [89,90]. Dissimilarly, the selected Cu 10–35 μm powder presents an improvement in densification, with a maximum value of 98.1 % at E_v of 1750 J/mm^3. While, as visible in Fig. 17, the melt pool behaviour retains some weld instability plus few lack of fusion defects are still expected, the finer distribution had demonstrated to be crucial to ease the laser melting process leading to relatively high density pure copper parts [31,34]. Appropriate LPBF production parameters must be considered, i.e. at lower energy densities than 1750 J/mm^3, if a reasonable volumetric material fabrication rate must be achieved. Production parameters were selected -in accordance with the LPBF machine manufacturer- at a scanning speed of 375 mm/s, with an expected copper part relative density as high as ~ 97 %. More information regarding mechanical/surface properties of the Cu 10–35 μm fabricated parts, and a first upscaling test for the LPBF production of massive pure copper components, are available in [31] being out of scope for the purpose of this present work.

2. CFD simulation of conjugate heat transfer with the ANSYS package

2.1. Meshing operations

The mesh generation exploited in this paper was based on the so-called *tetrahedrons patch independent algorithm*, a method which is particularly well suited for complex CAD geometries. This method creates a meshed volume incorporating the geometry to be discretized, and then adjust the various elements to match the mesh with the boundaries of the given geometry [91]. Such

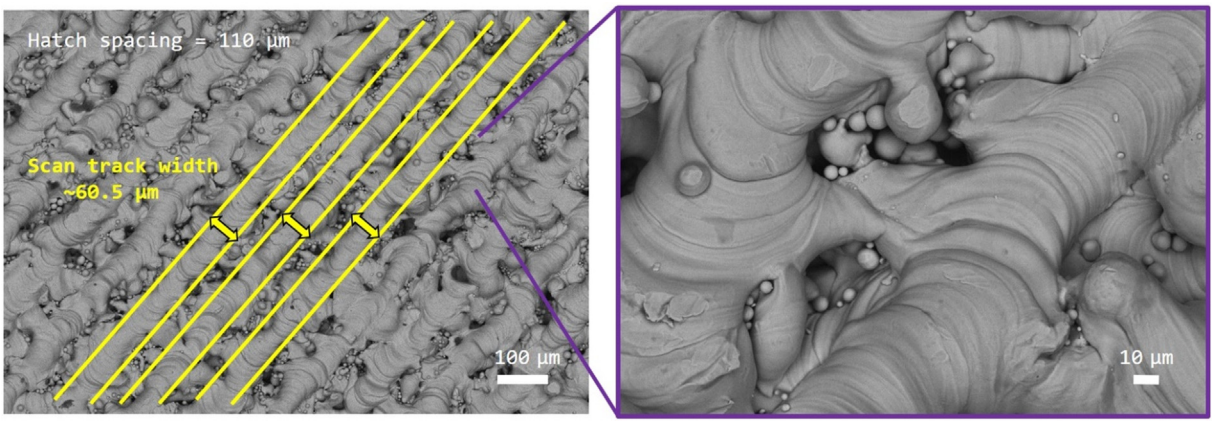

Fig. 17. left) Top surface SEM image of exemplifying sample fabricated with the Cu 10–35 µm powder and with intentionally increased hatch spacing of 110 µm, to appreciate the single scan tracks; right) zoomed-in section.

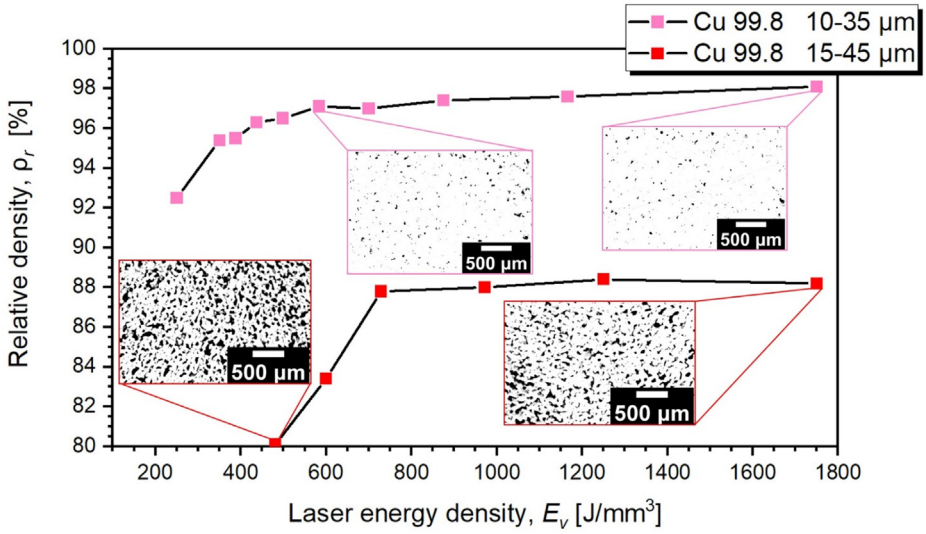

Fig. 18. LPBF performance comparison of the two Cu powders, relative densities are plotted as a function of Ev; exemplifying polished cross sections of selected specimens are included.

an approach gives the possibility to refine the mesh only in the critical zones, like in the proximity of the contact regions between fluid and solid. Regarding mesh quality, the most relevant indicator was found to be its *minimum orthogonal quality*: it was indeed observed that if this value is less than 0.1 the solution can be adversely affected from the point of view of convergence and correctness of results.

2.2. Turbulence and conjugate heat transfer modelling

When modelling turbulence, the equations of mass, momentum and energy conservation are solved following the Reynolds-Averaged Navier-Stokes (RANS) approach [92]. This involves the numerical resolution of the following equations:

$$\frac{\partial}{\partial x_i}\left(\rho\bar{u}_i\right) = 0 \tag{14}$$

$$\frac{\partial}{\partial x_i}\left(\rho\bar{u}_i\bar{u}_j\right) = -\frac{\partial \bar{p}}{\partial x_i} + \frac{\partial}{\partial x_j}\left[\mu\left(\frac{\partial \bar{u}_i}{\partial x_j} + \frac{\partial \bar{u}_j}{\partial x_i}\right) - \frac{2}{3}\delta_{ij}\frac{\partial \bar{u}_k}{\partial x_k}\right] + \frac{\partial}{\partial x_j}\left(-\rho\,\overline{u_i' u_j'}\right) \tag{15}$$

$$\frac{\partial \rho\bar{u}_i}{\partial x_i}\left(c_p T + \frac{1}{2}\bar{u}_i\bar{u}_i\right) = \frac{\partial}{\partial x_j}\lambda_{eff}\frac{\partial T}{\partial x_j} + \bar{u}_i\mu_{eff}\left[\left(\frac{\partial \bar{u}_i}{\partial x_j} + \frac{\partial \bar{u}_j}{\partial x_i}\right) - \frac{2}{3}\delta_{ij}\frac{\partial \bar{u}_k}{\partial x_k}\right] \tag{16}$$

In the above equations the following parameters appear:

- the fluid density ρ;
- the temperature T;
- the specific heat c_p;
- the Cartesian coordinates x_i, x_j, x_k;
- the Kronecker delta δ_{ij};
- the time-averaged $(\bar{u}_i, \bar{u}_j, \bar{u}_k)$ and fluctuating (u_i', u_j') velocity components;
- the time-averaged pressure $\bar{p}$;
- the effective thermal conductivity λ_{eff}, which value depends on the adopted turbulence model;
- the effective dynamic viscosity $\mu_{eff} = \mu + \mu_T$, with μ and μ_T the molecular and turbulent dynamic viscosity respectively.

In particular, a *k-ε* turbulence model [93] can be chosen to calculate the Reynolds stresses $-\rho\,\overline{u_i' u_j'}$, which offers a good balance

between accuracy and requirements in terms of computational costs in respect to other turbulence models. In its standard formulation, the transport equations for the turbulent kinetic energy k (17) and energy dissipation rate ε (18) are used to compute the Reynolds stresses through the Boussinesq expression (19) [94]:

$$\frac{\partial\left(\rho k\bar{u}_i\right)}{\partial x_j}=\frac{\partial}{\partial x_j}\left[\left(\mu+\frac{\mu_T}{\sigma_k}\right)\frac{\partial k}{\partial x_j}\right]-\rho\,\overline{u_i'u_j'}\,\frac{\partial\bar{u}_j}{\partial x_i}-\rho\varepsilon \tag{17}$$

$$\frac{\partial\left(\rho\varepsilon\bar{u}_i\right)}{\partial x_j}=\frac{\partial}{\partial x_j}\left[\left(\mu+\frac{\mu_T}{\sigma_\varepsilon}\right)\frac{\partial\varepsilon}{\partial x_j}\right]+C_{1\varepsilon}\frac{\varepsilon}{k}\left(-\rho\,\overline{u_i'u_j'}\,\frac{\partial\bar{u}_j}{\partial x_i}\right)-C_{2\varepsilon}\frac{\rho\varepsilon^2}{k} \tag{18}$$

$$-\rho\,\overline{u_i'u_j'}=\mu_T\left(\frac{\partial\bar{u}_i}{\partial x_j}+\frac{\partial\bar{u}_j}{\partial x_i}\right)-\frac{2}{3}\rho k\delta_{ij} \tag{19}$$

where $C_{1\varepsilon}$, $C_{2\varepsilon}$, σ_k and σ_ε are empirical constants.

In the *Re-Normalization Group* (RNG) variation [73] of standard k-ε, the quantity R_ε is added to the right-hand side of Eq. (18):

$$R_\varepsilon=-\frac{C_\mu\rho\eta^3\left(1-\frac{\eta}{\eta_0}\right)}{1+\beta\eta^3}\frac{\varepsilon^2}{k} \tag{20}$$

where $\eta = Sk/\varepsilon$, with $S=\sqrt{2S_{ij}S_{ij}}$ the modulus of the mean strain rate tensor [95], while $C_\mu = 0.0845$, as derived from the RNG theory, and $\eta_0 = 4.38$ and $\beta = 0.012$ as set in Fluent. This parameter allows for a correction in relation to the strain rate, thus considering the effects of rapidly changing flows. Moreover, the effective viscosity $\mu + \mu_T$ in both the k and ε transport equations is multiplied with the inverse turbulent Prandtl number α, determined by:

$$\left|\frac{\alpha-1.3929}{\alpha_0-1.3929}\right|^{0.6321}\left|\frac{\alpha+2.3929}{\alpha_0+2.3929}\right|^{0.3679}=\frac{\mu}{\mu_{eff}} \tag{21}$$

where here α_0 refers to the inverse molecular Prandtl number. In addition to this, in this model $\lambda_{eff} = \alpha c_p \mu_{eff}$, whereas, in the standard and *Realizable* [96] k-ε formulations, $\lambda_{eff} = \lambda + \alpha_t c_p \mu_T$, being λ the molecular thermal conductivity and α_t a constant inverse turbulent Prandtl number. By accounting for the influence of turbulence to the Prandtl number, the RNG formulation offers a more accurate prediction of the heat transfer with low Reynolds numbers.

Withal, regarding the modelling of the fluid behaviour at the wall-fluid boundary layer, the *scalable wall functions* avoid the need to adjust the thickness of the first layers of elements at the fluid boundaries. Indeed, this option introduces a low limit of 11.225 in the dimensionless distance from the wall y^*, which value continues to be determined with the standard wall function approach proposed in [93].

References

[1] I. Novak-Hofer, A.P. Schubiger, Copper-67 as a therapeutic nuclide for radioimmunotherapy, Eur. J. Nucl. Med. 29 (6) (2002) 821–830, https://doi.org/10.1007/s00259-001-0724-y.

[2] C. Müller, K.A. Domnanich, C.A. Umbricht, N.P. van der Meulen, Scandium and terbium radionuclides for radiotheranostics: current state of development towards clinical application, BJR 91 (1091) (2018) 20180074, https://doi.org/10.1259/bjr.20180074.

[3] J. Esposito, D. Bettoni, A. Boschi, M. Calderolla, S. Cisternino, G. Fiorentini, G. Keppel, P. Martini, M. Maggiore, L. Mou, M. Pasquali, L. Pranovi, G. Pupillo, C. Rossi Alvarez, L. Sarchiapone, G. Sciacca, H. Skliarova, P. Favaron, A. Lombardi, P. Antonini, A. Duatti, LARAMED: A Laboratory for Radioisotopes of Medical Interest, Molecules 24 (2018) 20, https://doi.org/10.3390/molecules24010020.

[4] M. Maggiore, D. Campo, P. Antonini, A. Lombardi, M. Manzolaro, A. Andrighetto, A. Monetti, D. Scarpa, J. Esposito, L. Silvestrin, SPES: A new cyclotron-based facility for research and applications with high-intensity beams, Mod. Phys. Lett. A 32 (17) (2017) 1740010, https://doi.org/10.1142/S0217732317400107.

[5] F. Haddad, Production de radionucléides et recherche sur les cibles, 2010. http://asso-lard.eu/wp-content/uploads/2010/08/LARD.pdf.

[6] Internationale Atomenergie-Organisation, ed., Standardized high current solid targets for cyclotron production of diagnostic and therapeutic radionuclides, Vienna, 2004.

[7] S.D. Warshaw, The Stopping Power for Protons in Several Metals, Phys. Rev. 76 (12) (1949) 1759–1765, https://doi.org/10.1103/PhysRev.76.1759.

[8] H. Thisgaard, M. Jensen, D.R. Elema, Medium to large scale radioisotope production for targeted radiotherapy using a small PET cyclotron, Appl. Radiat. Isot. 69 (1) (2011) 1–7, https://doi.org/10.1016/j.apradiso.2010.07.019.

[9] M.A. Rovais, K. Yousefi, K. Ardaneh, M. Mirzaii, Computer simulation of temperature distribution on a solid target for 201Tl production, Nukleonika 56 (2011) 283–289.

[10] M.G. Hur, S.D. Yang, S.W. Kim, I.J. Kim, S.M. Choi, High current solid target for radioisotope production at cyclotron using metal foam, U.S. Patent No. 8,867,686, 2014.

[11] C. Zhang, S. Wang, J. Li, Y.i. Zhu, T. Peng, H. Yang, Additive manufacturing of products with functional fluid channels: A review, Addit. Manuf. 36 (2020) 101490, https://doi.org/10.1016/j.addma.2020.101490.

[12] B.M. Nafis, R. Whitt, A.-C. Iradukunda, D. Huitink, Additive Manufacturing for Enhancing Thermal Dissipation in Heat Sink Implementation: A Review, Heat Transfer Eng. 42 (12) (2021) 967–984, https://doi.org/10.1080/01457632.2020.1766246.

[13] U. Scheithauer, R. Kordaß, K. Noack, M. F. Eichenauer, M. Hartmann, J. Abel, G. Ganzer, D. Lordick, Potentials and Challenges of Additive Manufacturing Technologies for Heat Exchanger, in: L. Castro Gómez, V. Manuel Velázquez Flores (Eds.), Advances in Heat Exchangers, IntechOpen, 2019. Doi: 10.5772/intechopen.80010.

[14] ISO/ASTM 52900:2021, (n.d.). https://www.iso.org/standard/74514.html (accessed December 10, 2021).

[15] W.E. Frazier, Metal Additive Manufacturing: A Review, J. Mater. Eng. Perform. 23 (6) (2014) 1917–1928, https://doi.org/10.1007/s11665-014-0958-z.

[16] S.L. Sing, W.Y. Yeong, Laser powder bed fusion for metal additive manufacturing: perspectives on recent developments, Virtual Phys. Prototyping. 15 (3) (2020) 359–370, https://doi.org/10.1080/17452759.2020.1779999.

[17] W. Ameen, A.M. Ghaleb, M. Alatefi, H. Alkhalefah, A. Alahmari, An overview of selective laser sintering and melting research using bibliometric indicators, Virtual Phys. Prototyping 13 (4) (2018) 282–291, https://doi.org/10.1080/17452759.2018.1489973.

[18] D. Jafari, W.W. Wits, The utilization of selective laser melting technology on heat transfer devices for thermal energy conversion applications: A review, Renew. Sustain. Energy Rev. 91 (2018) 420–442, https://doi.org/10.1016/j.rser.2018.03.109.

[19] Z. Ren, D.Z. Zhang, G. Fu, J. Jiang, M. Zhao, High-fidelity modelling of selective laser melting copper alloy: Laser reflection behavior and thermal-fluid dynamics, Mater. Des. 207 (2021) 109857, https://doi.org/10.1016/j.matdes.2021.109857.

[20] T.Q. Tran, A. Chinnappan, J.K.Y. Lee, N.H. Loc, L.T. Tran, G. Wang, V.V. Kumar, W. A.D.M. Jayathilaka, D. Ji, M. Doddamani, S. Ramakrishna, 3D Printing of Highly Pure Copper, Metals. 9 (2019) 756, https://doi.org/10.3390/met9070756.

[21] R. Gu, S.W. Kam, M. Yan, Laser additive manufacturing of typical highly reflective materials—gold, silver and copper, Sci. Sin.-Phys. Mech. Astron. 50 (2019), https://doi.org/10.1360/SSPMA-2019-0267 034204.

[22] M.R. Campagnoli, M. Galati, A. Saboori, On the processability of copper components via powder-based additive manufacturing processes: Potentials, challenges and feasible solutions, J. Manuf. Processes 72 (2021) 320–337.

[23] Q. Jiang, P. Zhang, Z. Yu, H. Shi, D. Wu, H. Yan, X. Ye, Q. Lu, Y. Tian, A Review on Additive Manufacturing of Pure Copper, Coatings 11 (2021) 740, https://doi.org/10.3390/coatings11060740.

[24] F. Singer, D.C. Deisenroth, D.M. Hymas, M.M. Ohadi, in: Additively manufactured copper components and composite structures for thermal management applications, IEEE, Orlando, FL, 2017, pp. 174–183, https://doi.org/10.1109/ITHERM.2017.7992469.

[25] Eos website, (n.d.). https://www.eos.info/en/additive-manufacturing/3d-printing-metal/dmls-metal-materials/copper (accessed December 10, 2021).

[26] S.D. Jadhav, L.R. Goossens, Y. Kinds, B.V. Hooreweder, K. Vanmeensel, Laser-based powder bed fusion additive manufacturing of pure copper, Addit. Manuf. 42 (2021) 101990, https://doi.org/10.1016/j.addma.2021.101990.

[27] Trumpf website, (n.d.). https://www.trumpf.com/en_INT/products/machines-systems/additive-production-systems/truprint-serie-1000-green-edition/ (accessed December 10, 2021).

[28] S.D. Jadhav, P.P. Dhekne, S. Dadbakhsh, J.-P. Kruth, J. Van Humbeeck, K. Vanmeensel, Surface Modified Copper Alloy Powder for Reliable Laser-based Additive Manufacturing, Addit. Manuf. 35 (2020) 101418, https://doi.org/10.1016/j.addma.2020.101418.

[29] S.D. Jadhav, D. Fu, M. Deprez, K. Ramharter, D. Willems, B. Van Hooreweder, K. Vanmeensel, Highly conductive and strong CuSn0.3 alloy processed via laser powder bed fusion starting from a tin-coated copper powder, Addit. Manuf. 36 (2020) 101607, https://doi.org/10.1016/j.addma.2020.101607.

[30] V. Lindström, O. Liashenko, K. Zweiacker, S. Derevianko, V. Morozovych, Y. Lyashenko, C. Leinenbach, Laser Powder Bed Fusion of Metal Coated Copper Powders, Materials 13 (2020) 3493, https://doi.org/10.3390/ma13163493.

[31] M. Sinico, G. Cogo, M. Benettoni, I. Calliari, A. Pepato, Influence of Powder Particle Size Distribution on the printability of Pure Copper for Selective Laser Melting, in: Proceedings of the 30th Annual International Solid Freeform Fabrication Symposium – An Additive Manufacturing Conference, SFF Symposium Proceedings, 2019: pp. 657–667. https://www.sffsymposium.org/, (accessed May 6, 2020).
[32] M. Sinico, A.A. Rossi, A. Pepato, Selective Laser Melting of Pure Copper at Low Laser Power, 2017. http://rgdoi.net/10.13140/RG.2.2.31674.90565/1 (accessed August 5, 2020).
[33] S. Vock, B. Klöden, A. Kirchner, T. Weißgärber, B. Kieback, Powders for powder bed fusion: a review, Prog. Additive Manuf. 4 (4) (2019) 383–397, https://doi.org/10.1007/s40964-019-00078-6.
[34] A.T. Sutton, C.S. Kriewall, M.C. Leu, J.W. Newkirk, Powder characterisation techniques and effects of powder characteristics on part properties in powder-bed fusion processes, Virtual Phys. Prototyping 12 (1) (2017) 3–29, https://doi.org/10.1080/17452759.2016.1250605.
[35] EOS GmbH Electro Optical Systems, Datasheet: EOS Copper Cu EOS M 290 | 20 µm, (2019). https://www.eos.info/03_system-related-assets/material-related-contents/metal-materials-and-examples/metal-material-datasheet/copper/material_datasheet_eos_copper_cu_core_en.pdf.
[36] S. Qu, J. Ding, J. Fu, M. Fu, B. Zhang, X.u. Song, High-precision laser powder bed fusion processing of pure copper, Addit. Manuf. 48 (2021) 102417, https://doi.org/10.1016/j.addma.2021.102417.
[37] G. Wang, Y. Gu, L. Zhao, J. Xuan, G. Zeng, Z. Tang, Y. Sun, Experimental and numerical investigation of fractal-tree-like heat exchanger manufactured by 3D printing, Chem. Eng. Sci. 195 (2019) 250–261, https://doi.org/10.1016/j.ces.2018.07.021.
[38] W.C. Yameen, N.A. Piascik, A.K. Miller, R.C. Clemente, J.Z. Benner, A.D. Santamaria, S.A. Niknam, M. Mortazavi, Modified Manifold-Microchannel Heat Exchangers Fabricated Based on Additive Manufacturing: Experimental Characterization, in: ASME 2019 Heat Transfer Summer Conference, American Society of Mechanical Engineers, Bellevue, Washington, USA, 2019: p. V001T07A002. Doi: 10.1115/HT2019-3535.
[39] B. Gürel, V.R. Akkaya, M. Göltaş, Ç.N. Şen, O.V. Güler, M.İ. Koşar, A. Keçebaş, Investigation on flow and heat transfer of compact brazed plate heat exchanger with lung pattern, Appl. Therm. Eng. 175 (2020) 115309, https://doi.org/10.1016/j.applthermaleng.2020.115309.
[40] M. Pelanconi, M. Barbato, S. Zavattoni, G.L. Vignoles, A. Ortona, Thermal design, optimization and additive manufacturing of ceramic regular structures to maximize the radiative heat transfer, Mater. Des. 163 (2019) 107539, https://doi.org/10.1016/j.matdes.2018.107539.
[41] T.W. Wei, H. Oprins, V. Cherman, E. Beyne, M. Baelmans, Experimental and numerical investigation of direct liquid jet impinging cooling using 3D printed manifolds on lidded and lidless packages for 2.5D integrated systems, Appl. Therm. Eng. 164 (2020) 114535, https://doi.org/10.1016/j.applthermaleng.2019.114535.
[42] Y.-C. Huang, H.-C. Hsu, Selective Laser Melting Heat Sinks under Jet Impingement Cooling for Heat Dissipation of Higher Light Output LED Lighting in a Limited Space, Appl. Sci. 10 (2020) 3898, https://doi.org/10.3390/app10113898.
[43] A. Seharing, A.H. Azman, S. Abdullah, A review on integration of lightweight gradient lattice structures in additive manufacturing parts 168781402091695, Adv. Mech. Eng. 12 (2020), https://doi.org/10.1177/1687814020916951.
[44] S. Catchpole-Smith, R.R.J. Sélo, A.W. Davis, I.A. Ashcroft, C.J. Tuck, A. Clare, Thermal conductivity of TPMS lattice structures manufactured via laser powder bed fusion, Addit. Manuf. 30 (2019) 100846, https://doi.org/10.1016/j.addma.2019.100846.
[45] D. Shamvedi, O.J. McCarthy, E. O'Donoghue, C. Danilenkoff, P. O'Leary, R. Raghavendra, 3D Metal printed heat sinks with longitudinally varying lattice structure sizes using direct metal laser sintering, Virtual Phys. Prototyping 13 (4) (2018) 301–310, https://doi.org/10.1080/17452759.2018.1479528.
[46] S.Y. Choy, C.-N. Sun, K.F. Leong, J. Wei, Compressive properties of Ti-6Al-4V lattice structures fabricated by selective laser melting: Design, orientation and density, Addit. Manuf. 16 (2017) 213–224, https://doi.org/10.1016/j.addma.2017.06.012.
[47] T. Maconachie, M. Leary, B. Lozanovski, X. Zhang, M.a. Qian, O. Faruque, M. Brandt, SLM lattice structures: Properties, performance, applications and challenges, Mater. Des. 183 (2019) 108137, https://doi.org/10.1016/j.matdes.2019.108137.
[48] Z. Ma, D.Z. Zhang, F. Liu, J. Jiang, M. Zhao, T. Zhang, Lattice structures of Cu-Cr-Zr copper alloy by selective laser melting: Microstructures, mechanical properties and energy absorption, Mater. Des. 187 (2020) 108406, https://doi.org/10.1016/j.matdes.2019.108406.
[49] L. Constantin, Z. Wu, N. Li, L. Fan, J.-F. Silvain, Y.F. Lu, Laser 3D printing of complex copper structures, Addit. Manuf. 35 (2020) 101268, https://doi.org/10.1016/j.addma.2020.101268.
[50] K. Cheng, W. Xiong, Y. Li, L. Hao, C. Yan, Z. Li, Z. Liu, Y. Wang, K. Essa, L.i. Lee, X. Gong, T. Peijs, In-situ deposition of three-dimensional graphene on selective laser melted copper scaffolds for high performance applications, Compos. A Appl. Sci. Manuf. 135 (2020) 105904, https://doi.org/10.1016/j.compositesa:2020.105904.
[51] M.o. Bai, J.N. Chung, Enhanced Cooling of a Liquid-Fueled Rocket Thrust Chamber by Metal Foams, J. Propul. Power 28 (2) (2012) 434–443.
[52] T.M. Kuzay, J.T. Collins, J. Koons, Boiling liquid nitrogen heat transfer in channels with porous copper inserts, Int. J. Heat Mass Transf. 42 (7) (1999) 1189–1204.
[53] I. Echeta, X. Feng, B. Dutton, R. Leach, S. Piano, Review of defects in lattice structures manufactured by powder bed fusion, Int. J. Adv. Manuf. Technol. 106 (5-6) (2020) 2649–2668, https://doi.org/10.1007/s00170-019-04753-4.
[54] D.i. Wang, Y. Yang, R. Liu, D. Xiao, J. Sun, Study on the designing rules and processability of porous structure based on selective laser melting (SLM), J. Mater. Process. Technol. 213 (10) (2013) 1734–1742, https://doi.org/10.1016/j.jmatprotec.2013.05.001.
[55] S. Feng, A.M. Kamat, S. Sabooni, Y. Pei, Experimental and numerical investigation of the origin of surface roughness in laser powder bed fused overhang regions, Virtual Phys. Prototyping 16 (sup1) (2021) S66–S84, https://doi.org/10.1080/17452759.2021.1896970.
[56] A. Hasanpour, M. Farhadi, K. Sedighi, A review study on twisted tape inserts on turbulent flow heat exchangers: The overall enhancement ratio criteria, Int. Commun. Heat Mass Transfer 55 (2014) 53–62, https://doi.org/10.1016/j.icheatmasstransfer.2014.04.008.
[57] M.G. Varun, Garg, H. Nautiyal, S. Khurana, M.K. Shukla, Heat transfer augmentation using twisted tape inserts: A review, Renew. Sustain. Energy Rev. 63 (2016) 193–225, https://doi.org/10.1016/j.rser.2016.04.051.
[58] M.H. Mousa, N. Miljkovic, K. Nawaz, Review of heat transfer enhancement techniques for single phase flows, Renew. Sustain. Energy Rev. 137 (2021) 110566, https://doi.org/10.1016/j.rser.2020.110566.
[59] J.D. Bernardin, K. Ferguson, D. Sattler, The Testing and Model Validation of an Additively Manufactured Twisted Tube Heat Exchanger, in: ASME 2019 Heat Transfer Summer Conference, American Society of Mechanical Engineers, Bellevue, Washington, USA, 2019: p. V001T07A001. Doi: 10.1115/HT2019-3500.
[60] B. Kwon, L. Liebenberg, A.M. Jacobi, W.P. King, Heat transfer enhancement of internal laminar flows using additively manufactured static mixers, Int. J. Heat Mass Transf. 137 (2019) 292–300, https://doi.org/10.1016/j.ijheatmasstransfer.2019.03.133.
[61] B. Cheng, S. Shrestha, K. Chou, Stress and deformation evaluations of scanning strategy effect in selective laser melting, Addit. Manuf. 12 (2016) 240–251, https://doi.org/10.1016/j.addma.2016.05.007.
[62] M. Moesen, T. Craeghs, J.-P. Kruth, J. Schrooten, Robust beam compensation for laser-based additive manufacturing, Comput. Aided Des. 43 (8) (2011) 876–888, https://doi.org/10.1016/j.cad.2011.03.004.
[63] S. Clijsters, T. Craeghs, M. Moesen, J.-P. Kruth, Optimization of thin wall structures in SLM, in: Direct Digital Manufacturing Conference, Date: 2012/03/14-2012/03/15, Location: Berlin, 2012.
[64] R. Vrána, D. Koutný, D. Paloušek, L. Pantělejev, J. Jaroš, T. Zikmund, J. Kaiser, Selective Laser Melting Strategy for Fabrication of Thin Struts Usable in Lattice Structures, Materials 11 (2018) 1763, https://doi.org/10.3390/ma11091763.
[65] M. Sokolov, A. Salminen, Methods for Improving Laser Beam Welding Efficiency, Phys. Procedia 56 (2014) 450–457, https://doi.org/10.1016/j.phpro.2014.08.148.
[66] G. Sciacca, H. Skliarova, D. Bigolaro, S. Cisternino, C.R. Alvarez, J. Esposito, A Flexible Experimental Setup for Target Heat Sinks Testing, LNL Ann. Rep. 258 (2019) 182–183.
[67] T.L. Bergman, F.P. Incropera, D.P. DeWitt, A.S. Lavine, Fundamentals of heat and mass transfer, John Wiley & Sons, 2011.
[68] W. Chauvenet, A Manual of Spherical and Practical Astronomy, Embracing the General Problems of Spherical Astronomy: The Special Applications to Nautical Astronomy, and the Theory and Use of Fixed and Portable Astronomical Instruments, 5th ed., J. B. Lippincott Company, Philadelphia, 1891.
[69] S.J. Kline, Describing uncertainty in single sample experiments, Mech. Eng. 75 (1953) 3–8.
[70] T.J. Lu, H.A. Stone, M.F. Ashby, Heat transfer in open-cell metal foams, Acta Mater. 46 (10) (1998) 3619–3635, https://doi.org/10.1016/S1359-6454(98)00031-7.
[71] A. Kopanidis, A. Theodorakakos, E. Gavaises, D. Bouris, 3D numerical simulation of flow and conjugate heat transfer through a pore scale model of high porosity open cell metal foam, Int. J. Heat Mass Transf. 53 (11-12) (2010) 2539–2550, https://doi.org/10.1016/j.ijheatmasstransfer.2009.12.067.
[72] T. Dixit, I. Ghosh, Simulation intricacies of open-cell metal foam fin subjected to convective flow, Appl. Therm. Eng. 137 (2018) 532–544, https://doi.org/10.1016/j.applthermaleng.2018.04.011.
[73] V. Yakhot, S.A. Orszag, Renormalization group analysis of turbulence. I. Basic theory, J. Sci. Comput. 1 (1) (1986) 3–51, https://doi.org/10.1007/BF01061452.
[74] Ansys Fluent 2020 R2 Manual, ANSYS Inc, 2020. ansyshelp.ansys.com (accessed October 10, 2020).
[75] Y.i. Zhu, L. Zhou, S. Wang, C. Zhang, C. Zhao, L. Zhang, H. Yang, On friction factor of fluid channels fabricated using selective laser melting, Virtual Phys. Prototyping. 15 (4) (2020) 496–509, https://doi.org/10.1080/17452759.2020.1823093.
[76] P.J. Roache, Perspective: A Method for Uniform Reporting of Grid Refinement Studies, J. Fluids Eng. 116 (1994) 405–413, https://doi.org/10.1115/1.2910291.
[77] G.M. Laskowski, J. Kopriva, V. Michelassi, S. Shankaran, U. Paliath, R. Bhaskaran, Q. Wang, C. Talnikar, Z. Wang, F. Jia, Future Directions of High-Fidelity CFD for Aero-Thermal Turbomachinery Research, in: Analysis and Design, in: 46th AIAA Fluid Dynamics Conference, 2016, https://doi.org/10.2514/6.2016-3322.
[78] P. Andreetto, F. Chiarello, F. Costa, A. Crescente, S. Fantinel, F. Fanzago, E. Konomi, P.E. Mazzon, M. Menguzzato, M. Segatta, G. Sella, M. Sgaravatto, S. Traldi, M. Verlato, L. Zangrando, A. Forti, L. Betev, M. Litmaath, O. Smirnova, P.

Hristov, Merging OpenStack-based private clouds: the case of CloudVeneto.it, EPJ Web Conf. 214 (2019) 07010, https://doi.org/10.1051/epjconf/201921407010.
[79] L. Eça, M. Hoekstra, A procedure for the estimation of the numerical uncertainty of CFD calculations based on grid refinement studies, J. Comput. Phys. 262 (2014) 104–130, https://doi.org/10.1016/j.jcp.2014.01.006.
[80] Z. Zhu, V.G. Dhokia, A. Nassehi, S.T. Newman, A review of hybrid manufacturing processes – state of the art and future perspectives, Int. J. Comput. Integr. Manuf. 26 (7) (2013) 596–615, https://doi.org/10.1080/0951192X.2012.749530.
[81] M. Merklein, D. Junker, A. Schaub, F. Neubauer, Hybrid Additive Manufacturing Technologies – An Analysis Regarding Potentials and Applications, Physics Procedia 83 (2016) 549–559, https://doi.org/10.1016/j.phpro.2016.08.057.
[82] C. Liu, D. Yan, J. Tan, Z. Mai, Z. Cai, Y. Dai, M. Jiang, P. Wang, Z. Liu, C.-C. Li, C. Lao, Z. Chen, Development and experimental validation of a hybrid selective laser melting and CNC milling system, Addit. Manuf. 36 (2020) 101550, https://doi.org/10.1016/j.addma.2020.101550.
[83] D. York, N.M. Evensen, M.L. Martínez, J. De Basabe Delgado, Unified equations for the slope, intercept, and standard errors of the best straight line, Am. J. Phys. 72 (3) (2004) 367–375, https://doi.org/10.1119/1.1632486.
[84] J.W. Slater, Examining Spatial (Grid) Convergence, NPARC Alliance CFD Verification and Validation Web Site. (2008). https://www.grc.nasa.gov/www/wind/valid/tutorial/spatconv.html (accessed January 23, 2021).
[85] F.M. White, Fluid Mechanics, 7th ed., McGraw Hill, New York, 2011.
[86] A. Hess, R. Schuster, A. Heider, R. Weber, T. Graf, Continuous Wave Laser Welding of Copper with Combined Beams at Wavelengths of 1030nm and of 515nm, Phys. Procedia 12 (2011) 88–94, https://doi.org/10.1016/j.phpro.2011.03.012.
[87] J.R. Davis, Copper and Copper Alloys, ASM Int. (2001).
[88] E. Weidmann, A. Guesnier, Metallographic preparation of copper and copper alloys, Struers ApS Application Notes, 2019
[89] P.A. Lykov, E.V. Safonov, A.M. Akhmedianov, Selective Laser Melting of Copper, MSF 843 (2016) 284–288, https://doi.org/10.4028/www.scientific.net/MSF.843.284.
[90] F. Trevisan, C. Flaviana, M. Diego, F. Paolo, Selective laser melting of chemical pure copper powders, in: Proceedings of the Euro PM2017 Congress & Exhibition, Milan, Italy, 2017. https://www.researchgate.net/publication/320372540_Selective_laser_melting_of_chemical_pure_copper (accessed May 3, 2018).
[91] Ansys Meshing 2020 R2 Manual, ANSYS Inc, 2020. ansyshelp.ansys.com (accessed October 10, 2020).
[92] H.K. Versteeg, W. Malalasekera, Computational fluid dynamics, The Finite Volume Method. (1995).
[93] B.E. Launder, D.B. Spalding, in: Numerical Prediction of Flow, Heat Transfer, Turbulence and Combustion, Elsevier, 1983, pp. 96–116, https://doi.org/10.1016/B978-0-08-030937-8.50016-7.
[94] J. Boussinesq, Essai sur la théorie des eaux courantes, Impr. nationale (1877).
[95] T.B. Gatski, M.Y. Hussaini, J.L. Lumley (Eds.), Simulation and Modeling of Turbulent FlowsSimulation and Modeling of Turbulent Flows, Oxford University Press, 1996.
[96] T.-H. Shih, W.W. Liou, A. Shabbir, Z. Yang, J. Zhu, A new k-ϵ eddy viscosity model for high reynolds number turbulent flows, Comput. Fluids 24 (3) (1995) 227–238, https://doi.org/10.1016/0045-7930(94)00032-T.